# Vertebrate kidney tubules elongate using a planar cell polarity–dependent, rosette-based mechanism of convergent extension

Soeren S Lienkamp[1], Kun Liu[2,3], Courtney M Karner[4,5], Thomas J Carroll[4,5], Olaf Ronneberger[2,3], John B Wallingford[6–8] & Gerd Walz[1,3]

**Cystic kidney diseases are a global public health burden, affecting over 12 million people[1]. Although much is known about the genetics of kidney development and disease, the cellular mechanisms driving normal kidney tubule elongation remain unclear[2,3]. Here, we used *in vivo* imaging to show for the first time that mediolaterally oriented cell intercalation is fundamental to vertebrate kidney morphogenesis. Unexpectedly, we found that kidney tubule elongation is driven in large part by a myosin-dependent, multicellular rosette–based mechanism, previously only described in *Drosophila melanogaster*. In contrast to findings in *Drosophila*, however, non-canonical Wnt and planar cell polarity (PCP) signaling is required to control rosette topology and orientation during vertebrate kidney tubule elongation. These data resolve long-standing questions concerning the role of PCP signaling in the developing kidney and, moreover, establish rosette-based intercalation as a deeply conserved cellular engine for epithelial morphogenesis.**

An outstanding challenge is to understand how the dynamic behavior of individual cells, acting collectively, remodels the developing kidney tubule epithelium and how defects in this process lead to cystogenesis. Although recent advances in imaging have begun to elucidate the mechanisms of branching morphogenesis in the kidney[4], a similar understanding of tubule elongation has not emerged. Mechanisms proposed for tubule elongation include convergent extension cell movements[5,6] and oriented cell divisions[7]. However, debate continues because tubule elongation is an inherently dynamic process, and previous studies have relied on the analysis of static images from fixed tissue[5–7]. A related and unanswered question in both normal kidney morphogenesis and the pathogenesis of kidney cysts concerns the role of the PCP signaling system[5,8]. PCP signaling is of particular interest, as it has been shown to govern both convergent extension and oriented cell division in a variety of

biological contexts[9]. In light of these two outstanding problems, we undertook studies to discern the mechanisms by which PCP signaling controls the dynamic behavior of kidney tubule epithelial cells during vertebrate development.

In a previous study, we proposed that PCP-mediated convergent extension drives kidney tubule elongation[5], but the cellular mechanism by which this convergent extension may occur remained unknown. Immunostaining of developing mice for E-cadherin at embryonic day (E) 15.5 identified the presence of multicellular rosettes in the kidney tubule collecting duct epithelium (**Fig. 1**). Such multicellular rosettes have been observed previously in vertebrate epithelia, but their function has remained unknown[10,11]. By contrast, the function of multicellular rosettes has been well defined in the *Drosophila* germ band epithelium, where such rosettes are essential for the cell rearrangements that drive convergent extension[12]. In that tissue, concerted shrinkage of mediolateral cell-cell boundaries leads to the formation of multicellular rosettes, which then resolve at a perpendicular angle. Thus, cells are repositioned in such a way as to elongate and narrow the tissue (**Fig. 1a,b**)[12].

Determining the function of multicellular rosettes in the kidney tubule epithelium requires dynamic analysis and live imaging of nephron elongation at single-cell resolution. To meet this challenge, we exploited a vertebrate animal model in which the molecular patterning of the embryonic nephron is highly conserved compared to mammals[13,14] and in which the large size of tissues and cells has consistently allowed exceptional access to individual-cell behaviors *in vivo*[15–17]. The embryonic kidney of the frog *Xenopus laevis* consists of only a single giant nephron (**Fig. 2a**), and its structural and functional segmentation compares well with that of mammalian nephrons (ref. 14 and **Supplementary Fig. 1**). Moreover, the tissue architecture of *Xenopus* kidney tubules during elongation reflects that of the mammalian kidney: cells align mediolaterally, and the number of cells spanning the tubular circumference decreases as the tubule elongates

[1]Department of Medicine, Renal Division, University of Freiburg Medical Center, Freiburg, Germany. [2]Image Analysis Laboratory, Department of Computer Science, University of Freiburg, Freiburg, Germany. [3]Centre for Biological Signalling Studies (BIOSS), Freiburg, Germany. [4]Department of Internal Medicine, Division of Nephrology, University of Texas Southwestern Medical Center, Dallas, Texas, USA. [5]Department of Molecular Biology, University of Texas Southwestern Medical Center, Dallas, Texas, USA. [6]Section of Molecular Cell and Developmental Biology, University of Texas at Austin, Austin, Texas, USA. [7]Institute for Cellular and Molecular Biology, University of Texas at Austin, Austin, Texas, USA. [8]Howard Hughes Medical Institute & Section of Molecular Cell and Developmental Biology, Austin, Texas, USA. Correspondence should be addressed to J.B.W. (wallingford@mail.utexas.edu) or G.W. (gerd.walz@uniklinik-freiburg.de).
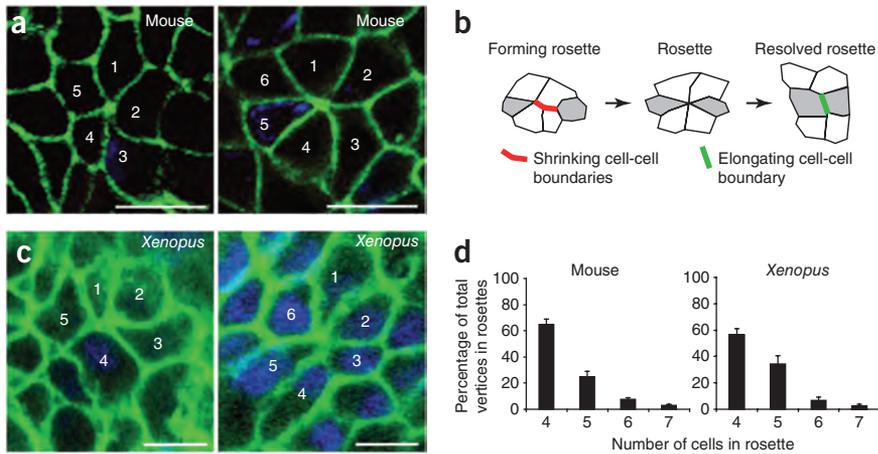
**Figure 1** Multicellular rosettes are conserved in mammalian kidney development. (**a**) Immunostaining for E-cadherin (green) in E15.5 mouse kidney collecting ducts shows the presence of multicellular rosettes (individual cells are numbered). Scale bars, 10 μm. (**b**) Diagram of rosette formation and resolution during morphogenesis in *Drosophila* germ band extension. The two cells for which cell rearrangement results in formation of a new common junction are shaded gray. (**c**) Immunostaining of fixed *Xenopus* tubules at stage 37 (antibody to membrane-targeted GFP, green; DAPI, blue) also detects rosettes. Individual cells are numbered. Scale bars, 10 μm. (**d**) Quantitative analysis of the fraction of vertices in rosette formation in mouse and *Xenopus* kidneys shows a similar distribution of rosette composition in both vertebrate species (*Xenopus*, n = 96 rosettes in 7 embryos; mouse, n = 263 rosettes in 3 embryos, collecting ducts). Error bars, s.e.m.

(**Fig. 2b–d**, **Supplementary Fig. 2** and **Supplementary Movie 1**). Notably, multicellular rosettes form in *Xenopus* kidney tubules, and the number of cells per rosette was similar in *Xenopus* and mouse (**Fig. 1c,d**). The parallels in functional segmentation, cellular architecture and rosette topology between *Xenopus* and mammals suggest that *Xenopus* will be a useful model for studying the dynamics of kidney tubule elongation.

We therefore developed a method for the *in vivo* imaging of kidney tubule elongation in *Xenopus* by combining targeted expression of membrane-tethered green fluorescent protein (GFP), confocal microscopy and custom software for image processing and analysis (**Supplementary Fig. 3** and **Supplementary Note**). Using this method, individual cells within the nephron could consistently be identified and tracked



over long periods of time *in vivo* (**Fig. 3a**, **Supplementary Fig. 4** and **Supplementary Movie 2**). We observed that cells within the elongating nephron underwent repeated rounds of intercalation (interdigitation) along the axis perpendicular to the elongating tubule. Such mediolateral cell intercalations were most apparent when rows of roughly adjacent cells were marked and followed over time (**Fig. 3b** and **Supplementary Movies 3** and **4**). Although suggested by previous work with fixed mammalian tissue[5], these results provide the first direct demonstration that vertebrate kidney tubules elongate by convergent extension and that this convergent extension is driven by planar polarized mediolateral cell intercalation.

Notably, our time-lapse data also confirmed that the multicellular rosettes observed in fixed tissue are, in fact, dynamic structures (**Fig. 3c,d** and **Supplementary Movie 5**). In *Drosophila*, such dynamic rosettes form and resolve in perpendicular orientation, thus driving the narrowing and elongation of the germ band (**Fig. 1b**)[12]. Consistent with a similar, causal role for multicellular rosettes in the morphogenesis of kidney tubules, the formation angle of rosettes that we observed was strongly biased mediolaterally, whereas the angle of rosette resolution was strongly biased perpendicularly, along the proximodistal axis (**Fig. 3e,f**). These data provide the first demonstration that multicellular rosette formation and resolution is a deeply conserved cellular mechanism associated with epithelial convergent extension in both insects and vertebrates.

In addition to the dynamics of multicellular rosettes, elongation of the *Drosophila* germ band is also driven in part by lower order (four-cell) polarized junctional remodeling events termed type 1 (shrinking junctions) to type 3 (expanding junctions) transitions (**Supplementary Fig. 5a**)[18,19]. We observed similar four-cell transitions in elongating kidney tubules, but, in contrast to the multicellular rosettes, the orientation of these transitions was not polarized at the stages observed (**Supplementary Fig. 5b,c**). In *Drosophila*, type 1 to type 3 transitions predominate early during germ band elongation, with multicellular rosettes predominating at later stages[12]; however, *in vivo* imaging at earlier stages of kidney development in *Xenopus* proved impossible due to higher tissue opacity. Our data

**Figure 2** Elongation of vertebrate kidney tubules by mediolateral cell intercalation. (**a**) Diagram of the structural similarities between the mammalian and amphibian nephron segments: G, glomerulus; PT, proximal tubule (yellow); LoH, loop of Henle (green); DT, distal tubule (orange); CT, connecting tubule (blue); CD, collecting duct (white); IT, intermediate tubule (green); CC, coelomic cavity (brown). The diagram was adapted, with permission, from ref. 14. (**b**) The morphology of the developing renal tubule in *Xenopus* visualized by staining for β-catenin (red; cell borders) and tomato lectin (green; tubule epithelium). Scale bars, 20 μm. Using three-dimensional visualization software, 20 cells in the intermediate tubule are volume rendered on the basis of cell borders (gray). The pronephric tubule is outlined by a dashed line. (**c**) Enlarged view of volume-rendered cells shown in **b**. Scale bars, 20 μm. (**d**) Cell outlines at the basal surface of the tubule. Arrows in the traced cells indicate the longest diameter at the basal side. Rose plots show that the angular distribution is biased toward the mediolateral axis with a length-to-width ratio (LWR) between 1.9 and 2.3. Top, proximal; bottom, distal (n = 42 cells in 3 to 4 embryos at each stage). The outer circle represents 50%, the middle circle 22% and the inner circle 4% of total observations. Scale bars, 20 μm.
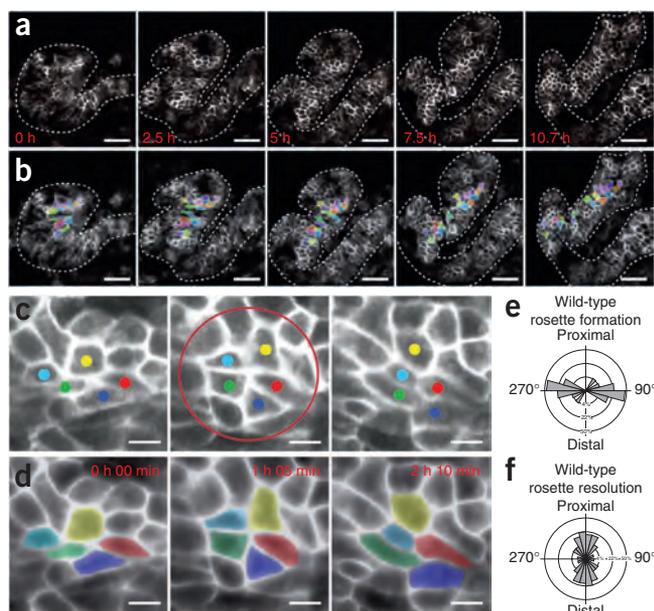
**Figure 3** Morphogenetic movements of renal tubule cells employs rosette formation. (**a**) Time-lapse confocal imaging and tracking of individual tubule cells show convergent extension movements within the developing kidney tubule in *Xenopus* (outlined by the dashed line; **Supplementary Movies 2** and **3**). Scale bars, 50 μm. (**b**) Cells were segmented and colored to visualize cell rearrangement over the course of 10.7 h. Scale bars, 50 μm. (**c**) Layer-extracted still images of a forming and resolving rosette (red circle) from time-lapse recordings (**Supplementary Movies 2** and **3**). Top, proximal; bottom distal. Scale bars, 10 μm. (**d**) Corresponding images to those in **c**, filtered and colored, showing rosette formation and resolution. (**e**,**f**) Rose plots show the angular distribution of 33 forming and resolving rosettes in 3 tubules. There is a significant difference between the distribution of formation and resolution angles ($P < 0.01$, Mardia-Watson-Wheeler test). The outer circle represents 50%, the middle circle 22% and the inner circle 4% of total observations. Rosettes form predominantly in a mediolateral angle (**e**), whereas resolution is biased toward a proximodistal angle (**f**).

four-cell transitions are under independent molecular control in the kidney tubules, consistent with recent data from *Drosophila*[20].

Our time-lapse data identify rosette behaviors in the developing vertebrate kidney that are markedly similar to those observed in the *Drosophila* germ band. However, rosettes in *Drosophila* have been characterized by focusing on the apical surface, whereas, for technical reasons, our imaging approach requires a focus on more basal regions. We therefore sought to perform mechanistic studies to advance our comparison of kidney tubule rosette behaviors in *Xenopus* to those in *Drosophila* (**Fig. 4**). Rosette-based intercalation in *Drosophila* requires the mediolaterally polarized action of

therefore suggest a key role for multicellular rosettes at the stages examined, although we cannot rule out a role for type 1 to type 3 transitions earlier in development. These results are especially noteworthy because they suggest that multicellular rosette formation and

**Figure 4** Inhibition of myosin interferes with cell movement in *Xenopus* tubule formation. (**a**,**b**) Immunostaining for S20-phosphorylated myosin light chain (pS20-MLC) (**a**) and *Lycopersicon esculentum* (tomato) lectin, which stains the membrane of tubule epithelial cells (**b**). Scale bars, 20 μm. (**c**) Densitometric analysis showed that the strongest signal of activated myosin light chain is detected at mediolaterally (ML) oriented cell junctions. Cell borders were categorized into six groups with angles between 0 and 180 degrees; pS20-MLC intensity was normalized against that of tomato lectin in ten kidney tubules (PD, posterodistal) and is significantly different from a random distribution ($P = 0.05$, ANOVA, $n = 312$ junctions). Error bars, s.e.m. (**d**,**e**) Parallel *in vivo* time-lapse analysis of embryos treated with DMSO (**d**) versus blebbistatin (**e**) shows disrupted cell rearrangement during tubule morphogenesis in those treated with blebbistatin. Colored tracks show the displacement of cells over time (up to 3 h). Crosses indicate cells that could not be tracked to the last frame. Scale bars, 20 μm. (**f**) Quantification of the number of cells participating in newly formed higher order rosettes (with five or more cells). Rosette detection was aided by a computerized algorithm on filtered images (**Supplementary Movies 4** and **5**) (difference in rosette frequency for all time points, $P < 0.001$, $t$ test, $n = 4$ embryos, 721 cells analyzed in DMSO-treated group, 1,341 cells analyzed in blebbistatin-treated group). Error bars, s.e.m. (**g**,**h**) Treatment with blebbistatin between stages 33 and 37 (tomato lectin–FITC, green; DAPI, blue) prevented elongation and narrowing of the renal tubule (**h**) relative to treatment with DMSO (**g**). Dashed lines indicate the position of the cross-sections taken for measurements. The yellow lines indicate the anatomical landmarks used for measuring tubule length (the fusion point of the nephrostomes to the anterior bending of the intermediate tubule). Scale bars, 50 μm. (**i**) The complexity of multicellular rosettes was reduced by treatment with blebbistatin in fixed *Xenopus* tubules ($n = 9$ tubules in DMSO-treated group, $n = 10$ tubules in blebbistatin-treated group). *$P < 0.01$, $t$ test. Error bars, s.e.m.
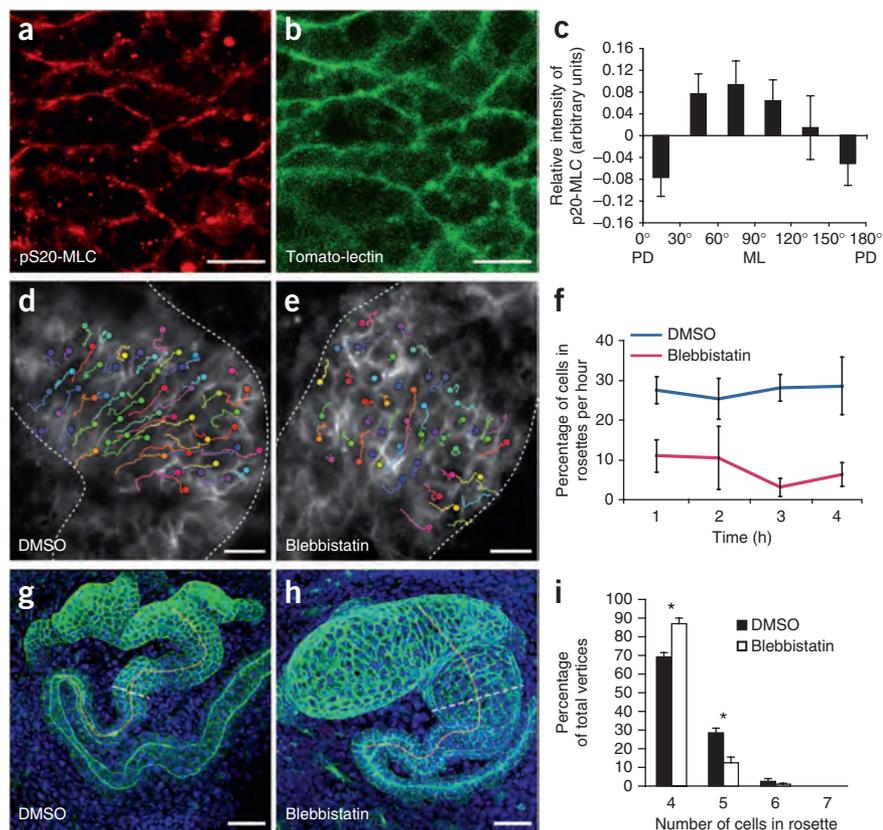
**Figure 5** PCP signaling controls polarized resolution of multicellular rosettes in developing vertebrate kidney tubules. (**a**) Unilateral expression of dexamethasone (dexa)-inducible Xdd1 (Xdd1-GR) resulted in shorter and wider tubules than in the uninjected, control side in *Xenopus* embryos (tomato lectin–FITC, green). The uninjected side is shown as a mirror image. Scale bars, 50 µm. (**b**) Quantification of tubules shows significantly larger diameter, increased number of cells and decreased tubule length in treated embryos (*n* = 15 GFP-GR embryos, *n* = 10 Xdd1-GF embryos). *P* < 0.05, *t* test. Error bars, s.e.m. (**c**) Time-lapse imaging of tubule cells shows that rosette formation and resolution are disrupted by Xdd1 (top). Filtered and colored images show rosettes forming and resolving cells (bottom and **Supplementary Movie 8**). In each image, top, proximal; bottom, distal. Scale bars, 10 µm. (**d**,**e**) Rose plots of the angular distribution of forming (**d**) and resolving (**e**) rosettes (*n* = 30 rosettes in 4 tubules). The outer circle represents 50%, the middle circle 22% and the inner circle 4% of total observations. (**f**) Analysis of junctional remodeling over a 30-min interval in a wild-type tubule. Shrinking (top) and expanding (bottom) junctions are marked. Scale bars, 20 µm. (**g**) The angular distribution of wild-type shrinking junctions is mediolaterally biased. The blue arrow represents the length of the mean vector *r* (*n* = 82 junctions in 3 embryos). (**h**) The distribution of expanding junctions is significantly less biased than that of shrinking junctions (*P* < 0.05, Mardia-Watson-Wheeler test, *n* = 96 junctions in 3 embryos). (**i**) In Xdd1-expressing tubules, shrinking junctions are mediolaterally biased (*n* = 118 junctions in 3 embryos). (**j**) The distribution of expanding junctions in Xdd1-expressing cells is not random but biased mediolaterally (*n* = 116 junctions in 3 embryos).
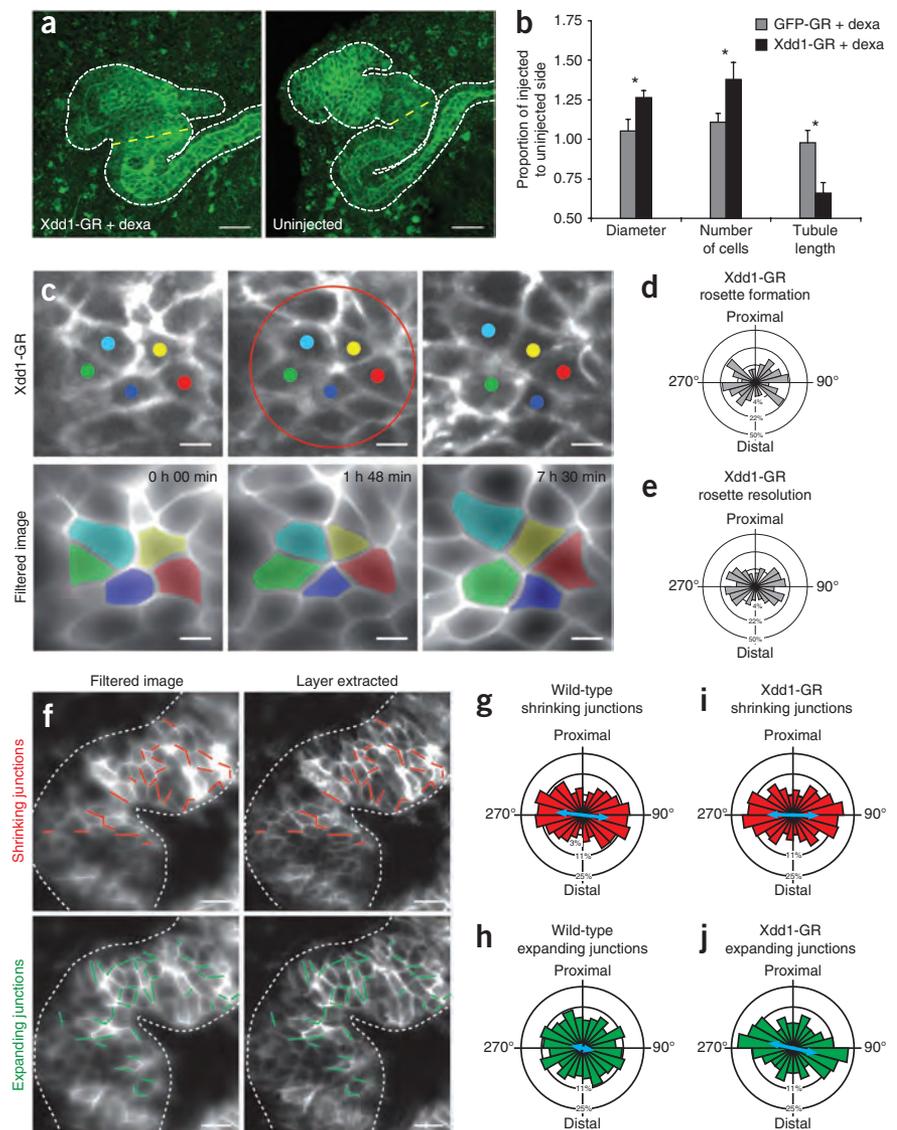


non-muscle myosin II (ref. 12). Accordingly, immunostaining showed that active (phosphorylated) myosin II was likewise enriched specifically along mediolaterally oriented cell-cell boundaries in the elongating kidney epithelium *in vivo* (**Fig. 4a–c** and **Supplementary Fig. 6**). Moreover, treatment with the myosin II inhibitor blebbistatin[21] markedly decreased both the number of multicellular rosettes (**Fig. 4f** and **Supplementary Movies 6** and **7**) and the topological complexity of these rosettes (**Fig. 4i**). Notably, these defects were associated with failed nephron morphogenesis (**Fig. 4g**,**h**). Tubule length in blebbistatin-treated embryos was shorter than in controls, whereas tubule diameter and the number of cells spanning the tubule circumference were significantly greater, consistent with a defect in convergent extension (**Supplementary Fig. 6**). Apical-basal epithelium height was not significantly changed (**Supplementary Fig. 6e**), suggesting a specific role for myosin II in cell rearrangements. Finally, *in vivo* time-lapse imaging showed that blebbistatin suppressed the mediolateral cell intercalations normally observed in kidney tubules at these stages (**Fig. 4d**,**e** and **Supplementary Fig. 6f**). Taken together, these data demonstrate that myosin-dependent, rosette-based cell intercalation is an ancient cellular mechanism for convergent extension and that it is employed by the elongating vertebrate nephron.

This deep conservation of a rosette-based mechanism driving convergent extension is quite unexpected and is at odds with the

observation that PCP signaling controls kidney tubule elongation[5,8,22], as mutations affecting core PCP proteins do not disrupt rosette-based cell intercalation in *Drosophila*[23]. To explore the link between PCP signaling and multicellular rosette formation, we initially examined mice with a conditional deletion of *Wnt9b* in the kidney tubules. These mice show defects in PCP-mediated kidney tubule convergent extension[5], and, notably, we found that they also showed a significant reduction in the topological complexity of multicellular rosettes. In wild-type, control kidneys, roughly 30% of observed rosettes contained five cells, 7% contained six cells and 2% contained seven cells (**Fig. 1d** and **Supplementary Fig. 7a**). Loss of *Wnt9b* completely eliminated seven-cell rosettes and reduced the numbers of five- and six-cell rosettes in the mouse kidney tubules; the number of four-cell vertices increased correspondingly (**Supplementary Fig. 7a**). Because such reductions in the topological complexity of multicellular rosettes consistently correlate with defective tissue elongation in *Drosophila*[12,20], the similar correlation in mouse kidney tubules suggested a potential link between PCP signaling, multicellular rosette topological complexity and convergent extension.

To further explore this hypothesis, we inhibited PCP signaling in the *Xenopus* kidney, specifically during the period of tubule elongation,

using targeted expression of a hormone-inducible version of Xdd1, a PCP-specific dominant-negative form of dishevelled-2 (**Fig. 5** and **Supplementary Fig. 8**). This approach elicited a significant reduction in nephron elongation, as well as corresponding increases in tubule diameter and the number of cells spanning the tubule circumference (**Fig. 5a,b**), defects that parallel those observed in *Wnt9b*-mutant mice (**Supplementary Fig. 9**)[5]. Notably, expression of Xdd1 disrupted rosette topology in *Xenopus* in a manner mirroring that seen with loss of *Wnt9b* in the mouse (**Supplementary Fig. 7a,b**).

In light of the similar topology defects with PCP disruption in both animals, we turned again to live imaging in *Xenopus* to better understand the role of PCP signaling in the dynamic control of multicellular rosettes. *In vivo* imaging of the *Xenopus* kidney tubules showed that disruption of PCP signaling not only elicited defects in topology but also disrupted the orientation of multicellular rosettes. After expression of Xdd1, the angle of rosette formation was significantly less biased toward the mediolateral axis than were the corresponding angles in control embryos expressing membrane-targeted GFP alone (**Fig. 5d**). Far more notable, however, was the observation that resolving rosettes completely failed to orient along the long axis of the tubule (**Fig. 5e** and **Supplementary Movie 8**). Indeed, most rosettes resolved in the same mediolateral orientation in which they formed (**Fig. 5c**).

In *Drosophila*, rosette formation occurs when a group of cells coordinately shrink their mediolaterally oriented cell-cell boundaries, whereas rosette resolution involves coordinate elongation of proximodistally oriented boundaries (**Fig. 1a**)[12]. We therefore assessed the effect of PCP disruption on the orientation of shrinking and elongating cell-cell boundaries in the developing kidney tubule epithelium. In the nephron, as in *Drosophila* germ band epithelium[18,19]. Shrinking cell-cell boundaries were strongly oriented along the mediolateral axis (**Fig. 5f,g**), whereas expanding junctions were more randomly distributed, with many boundaries expanding proximodistally (**Fig. 5f,h**). Notably, we found that Xdd1 expression did not significantly affect the orientation of shrinking boundaries but strongly suppressed any proximodistally oriented boundary elongation (**Fig. 5i,j**).

In summary, the data here provide, for the first time to our knowledge, a dynamic demonstration of the cellular basis of vertebrate kidney tubule elongation. These results are important in establishing the multicellular rosette mechanism for cell intercalation as a deeply conserved cellular engine for epithelial morphogenesis. Moreover, our data also show for the first time that in vertebrates this morphogenetic engine is under the control of an equally ancient molecular polarizing system, the PCP network. We find that, in the kidney tubule epithelium, PCP proteins control both the topology of rosettes and the ability of rosettes to resolve in an orientation perpendicular to their formation. These phenotypes suggest a role for PCP signaling in governing the action of myosin II because we found that myosin II is essential for rosette formation in the kidney, as it is in the *Drosophila* epithelium. Indeed, PCP signaling has previously been linked to myosin II activation in *Drosophila* and *Caenorhabditis elegans*[24,25].

Finally, by showing directly that vertebrate kidney tubules elongate by convergent extension cell movements, our live-imaging studies resolve an important and outstanding question in kidney morphogenesis. Our data strongly suggest that similar mechanisms act to drive kidney tubule elongation in *Xenopus* and mouse and thus can explain the elongation of kidney tubules during prenatal stages when the orientation of cell divisions is not aligned[5]. Thus, defects in rosette-based intercalation suggest a likely etiology for congenital kidney cyst formation associated with defective PCP signaling. Finally,

increased cell intercalations have been proposed to restore normal tubule diameter in mouse models with cysts arising from defects in oriented cell division[6]. As such, our new insights into the cellular basis of intercalation shed new light on a mechanism that could potentially be manipulated for therapeutic purposes.

**URLs.** ImageJ, http://rsbweb.nih.gov/ij/.

## METHODS
Methods and any associated references are available in the online version of the paper.

*Note: Supplementary information is available in the online version of the paper.*

### AUTHOR CONTRIBUTIONS
S.S.L., C.M.K., T.J.C., J.B.W. and G.W. designed the experiments, S.S.L., K.L., C.M.K. and O.R. performed experiments. S.S.L., K.L., C.M.K., T.J.C., O.R., J.B.W. and G.W. analyzed the data and wrote the manuscript.

1. Torres, V.E., Harris, P.C. & Pirson, Y. Autosomal dominant polycystic kidney disease. *Lancet* **369**, 1287–1301 (2007).
2. McNeill, H. Planar cell polarity and the kidney. *J. Am. Soc. Nephrol.* **20**, 2104–2111 (2009).
3. Chapin, H.C. & Caplan, M.J. The cell biology of polycystic kidney disease. *J. Cell Biol.* **191**, 701–710 (2010).
4. Costantini, F. Renal branching morphogenesis: concepts, questions, and recent advances. *Differentiation* **74**, 402–421 (2006).
5. Karner, C.M. *et al.* Wnt9b signaling regulates planar cell polarity and kidney tubule morphogenesis. *Nat. Genet.* **41**, 793–799 (2009).
6. Nishio, S. *et al.* Loss of oriented cell division does not initiate cyst formation. *J. Am. Soc. Nephrol.* **21**, 295–302 (2010).
7. Fischer, E. *et al.* Defective planar cell polarity in polycystic kidney disease. *Nat. Genet.* **38**, 21–23 (2006).
8. Saburi, S. *et al.* Loss of Fat4 disrupts PCP signaling and oriented cell division and leads to cystic kidney disease. *Nat. Genet.* **40**, 1010–1015 (2008).
9. Goodrich, L.V. & Strutt, D. Principles of planar polarity in animal development. *Development* **138**, 1877–1892 (2011).
10. Nishimura, T. & Takeichi, M. Shroom3-mediated recruitment of Rho kinases to the apical cell junctions regulates epithelial and neuroepithelial planar remodeling. *Development* **135**, 1493–1502 (2008).
11. Wagstaff, L.J., Bellett, G., Mogensen, M.M. & Munsterberg, A. Multicellular rosette formation during cell ingression in the avian primitive streak. *Dev. Dyn.* **237**, 91–96 (2008).
12. Blankenship, J.T., Backovic, S.T., Sanny, J.S., Weitz, O. & Zallen, J.A. Multicellular rosette formation links planar cell polarity to tissue morphogenesis. *Dev. Cell* **11**, 459–470 (2006).

13. Jones, E.A. *Xenopus*: a prince among models for pronephric kidney development. *J. Am. Soc. Nephrol.* **16**, 313–321 (2005).
14. Raciti, D. *et al.* Organization of the pronephric kidney revealed by large-scale gene expression mapping. *Genome Biol.* **9**, R84 (2008).
15. Wallingford, J.B. *et al.* Dishevelled controls cell polarity during *Xenopus* gastrulation. *Nature* **405**, 81–85 (2000).
16. Kieserman, E.K., Glotzer, M. & Wallingford, J.B. Developmental regulation of central spindle assembly and cytokinesis during vertebrate embryogenesis. *Curr. Biol.* **18**, 116–123 (2008).
17. Kim, S.K. *et al.* Planar cell polarity acts through septins to control collective cell movement and ciliogenesis. *Science* **329**, 1337–1340 (2010).
18. Bertet, C., Sulak, L. & Lecuit, T. Myosin-dependent junction remodelling controls planar cell intercalation and axis elongation. *Nature* **429**, 667–671 (2004).
19. Rauzi, M., Lenne, P.F. & Lecuit, T. Planar polarized actomyosin contractile flows control epithelial junction remodelling. *Nature* **468**, 1110–1114 (2010).
20. Tamada, M., Farrell, D.L. & Zallen, J.A. Abl regulates planar polarized junctional dynamics through β-catenin tyrosine phosphorylation. *Dev. Cell* **22**, 309–319 (2012).
21. Straight, A.F. *et al.* Dissecting temporal and spatial control of cytokinesis with a myosin II inhibitor. *Science* **299**, 1743–1747 (2003).
22. Lienkamp, S. *et al.* Inversin relays Frizzled-8 signals to promote proximal pronephros development. *Proc. Natl. Acad. Sci. USA* **107**, 20388–20393 (2010).
23. Zallen, J.A. & Wieschaus, E. Patterned gene expression directs bipolar planar polarity in *Drosophila*. *Dev. Cell* **6**, 343–355 (2004).
24. Winter, C.G. *et al.* *Drosophila* Rho-associated kinase (Drok) links Frizzled-mediated planar cell polarity signaling to the actin cytoskeleton. *Cell* **105**, 81–91 (2001).
25. Lee, J.Y. *et al.* Wnt/Frizzled signaling controls *C. elegans* gastrulation by activating actomyosin contractility. *Curr. Biol.* **16**, 1986–1997 (2006).

## ONLINE METHODS

***Xenopus* culture and microinjections.** Oocytes obtained from hormone-induced *Xenopus* females were fertilized *in vitro*. Embryos were cultured in 0.3× Marc's modified Ringer (MMR; 100 mM NaCl, 2 mM KCl, 2 mM CaCl$_2$, 1 mM MgCl$_2$, 5 mM HEPES, pH 7.4)). Injections with mRNA were performed in blastomeres C2 and C3 at the 8- to 32-cell stage. The inducible Xdd1 construct (Xdd1-GFP-GR) was cloned by inserting the sequence encoding Xdd1 into a modified pCS2+MT-GR vector (a gift from E.J. Bellefroid) and by replacing the sequence encoding the Myc tag with one encoding GFP. To induce Xdd1 activation, embryos were cultured in 10 µM dexamethasone in 0.2% ethanol in 0.3× MMR from stages 33 to 37. Plasmids were linearized with NotI, and mRNA was *in vitro* transcribed using the SP6 mMessage mMachine kit (Ambion). The institutional animal committee of the University Hospital Freiburg and the local authorities (Regierungspräsidium Baden-Württemberg, Germany) approved all experiments.

**Immunostaining and analysis.** *Xenopus* embryos were fixed at the indicated stages in MEMFA (0.1 M MOPS, 2 mM EGTA, 1 mM MgSO$_4$, 3.7% formaldehyde, pH 7.4) and stained with primary antibodies to β-catenin (Santa Cruz Biotechnology, sc-7199), phosphorylated histone H3 (Santa Cruz Biotechnology, sc-8656-R) or phosphorylated S20 myosin light chain (Abcam, ab2480) and Alexa Fluor 488–conjugated secondary antibody to rabbit (Invitrogen) or Cy3-conjugated secondary antibody to mouse (Jackson ImmunoResearch) or with fluorescein-coupled *L. esculentum* (tomato) lectin (Vector Laboratories). We used 4′,6-diamidino-2-phenylindole (DAPI) to stain nuclei. After dehydration in methanol, embryos were cleared in Murray's clear (2 parts benzyl benzoate and 1 part benzyl alcohol) and imaged on an inverted Zeiss 5 LIVE DuoScan microscope using a 40× oil immersion objective. Three-dimensional reconstruction, cell rendering and optical cross-sectioning were performed in Imaris Version 7.1 (Bitplane). Mouse kidney tubules were processed and stained as described[5]. Antibody to rat E-cadherin (Zymed, 13-1900; 1:500 dilution) was used to label cell membranes.

**Time-lapse confocal imaging and image analysis.** Embryos were treated with 0.0003% 1-phenyl-2-thiourea (PTU) after hatching to inhibit pigment formation. Stage 35 or 36 embryos were incubated in 0.3× MMR containing 0.0003% PTU and 0.01% ethyl 3-aminobenzoate, methanesulfonic acid salt (MS-222) for time-lapse analysis. Embryos were kept in 2- × 9-well µ-Slides (ibidi), and confocal imaging was performed on an inverted Zeiss LSM 4 microscope equipped with a movable table and a 25× glycerol immersion objective (numerical aperture (NA) of 0.8). The MultiTime Macro[26] or a customized macro for tracing moving objects was employed to correct for growth and sudden movement and for parallel recording of multiple embryos. For blebbistatin treatment, cells were labeled with membrane-targeted red fluorescent protein (memRFP) to avoid cytotoxicity[27]. We added 2% DMSO or 200 µM blebbistatin in 2% DMSO 30 min before recording in two-chamber slides (ibidi) for parallel imaging. Confocal stacks were acquired at 3- to 5-min intervals.

Huygens Professional (Scientific Volume Imaging) and Imaris (Bitplane) were used for image analysis in addition to customized algorithms. For rosette angle measurements, participating cells were labeled and were followed forward and backward in time to detect changes in the relative positioning of cells. Connecting lines between the two most distant cells relative to the tubular lumen were defined as the formation and resolution angles and were measured with ImageJ software on snapshot images. For measurement of angles and length-width ratios, ImageJ software was used.

**Heartbeat compensation.** In later developmental stages, the heartbeat of the embryo leads to periodic slight deformations of the whole sample. Due to the confocal scanning pattern, this produces severe discontinuities of the structures in the *z* direction (**Supplementary Fig. 10a**). We compensated for these discontinuities by an elastic deformation of each slice, where, for each pair of consecutive slices, the pixel correspondences were found by a dense diffeomorphic registration[28]. The results with this correction are shown in **Supplementary Figure 10b**. Details are given in the **Supplementary Note**.

**Cell border enhancement and decreasing noise.** Because the cell border is a plane-like structure in three dimensions, we made use of anisotropic diffusion to enhance local consistency in structure and suppress noise. The diffusion tensor, which enhances plane-like structures, is constructed from the local Hessian matrix. The results with this correction are depicted in **Supplementary Figure 11**. Further details are given in the **Supplementary Note**.

**Cell layer extraction.** The visible cells of the kidney tubule build a curved single-cell layer. To ease further analysis, this layer was projected into a two-dimensional image. A standard maximum-intensity projection (**Supplementary Fig. 12a**) is suboptimal and hides important details, especially in regions where the cell borders are not perpendicular to the viewing direction. Therefore, we instead estimated the position of the tubule cell layer (**Supplementary Fig. 12b**) by searching for sharp edges and cut a single curved slice from the data set (**Supplementary Fig. 12c,d**). In the extracted slice (**Supplementary Fig. 12e**), all cell borders were clearly visible. Further details are given in the **Supplementary Note**.

**Drift compensation (stabilization).** The growing embryo moves over time. This movement must be compensated for in the analysis. The displacement of two successive data sets is estimated by a normalized cross-correlation of their maximum-intensity projections. Stabilization of the whole time series is then performed by transforming each frame with the cumulative displacements. Further details are given in the **Supplementary Note**.

**Semiautomated cell tracking.** Cell tracking was performed on the stabilized cell layer slices that were extracted from the filtered images. Tracking backward in time helps to avoid the ambiguities that appear as a consequence of cell divisions. The cell centers in the last frame were extracted by searching for local gray-value minima in the filtered images, which have a minimum distance of the minimal cell diameter (here, 4 µm). The detector was restricted to the desired tubular structures by a manually defined mask. The few erroneous detections (false positives and false negatives) were manually corrected. Each cell center was tracked backward in time by searching for the trajectory that gave the best compromise between following the dense optical flow (computed either via high-accuracy optical flow[29] or diffeomorphic registration[28]) and passing through the local gray-value minima. In a final validation step, all trajectories were manually inspected and corrected, if necessary. Further details are given in the **Supplementary Note**.

**Segmentation.** Automatic segmentation was generated by a marker-controlled watershed algorithm, using the tracked cell centers as seed points. However, segmentation from the simple watershed was not sufficiently accurate in most frames. To improve segmentation, temporal consistency was explored. On the basis of flow vectors computed for semiautomated cell tracking, segmentations were aligned and examined for consistency in consecutive frames. A simple voting scheme was implemented to decide the correct segmentation from one frame and its neighboring frames. This procedure made cell segmentation nearly perfect for most regions with normal contrast (**Supplementary Fig. 13**). Finally, segmentation was further refined, for the relevant regions, by manually guiding the marker-controlled watershed through a graphical user interface (GUI) to correct some mislocated cell borders.

**Rosette detection.** Rosettes were defined as a configuration of at least five cells that shared a vertex with a maximum length of 3 µm (**Supplementary Fig. 14a,b**, white circle). We developed a fully automated method for rosette detection that works directly on the filtered cell layer images and does not rely on the cell tracking and marker-controlled segmentation steps.

In the first step, candidates for rosette centers are identified in an oversegmented image (**Supplementary Fig. 14c**). The oversegmentation is created by standard watershed segmentation on the filtered cell layer image. By assuming that the oversegmentation always produces one or more segments per cell but never accidently joins two cells of a rosette, we can reliably find all rosette center candidates, requiring that (i) the rosette center must be located close to a watershed line (here, a maximal distance of 1 µm was selected); (ii) there are five or more different segments in a circle (radius = 5.25 µm) surrounding the rosette center (**Supplementary Fig. 14d**); and (iii) the image intensity at the rosette center is higher than a threshold that is determined by the Otsu method[30] on the full image.

For all rosette center candidates, the surrounding image patch (extracted from the raw image) was compared to a rosette model that consisted of five (or more) radial rays (**Supplementary Fig. 14f–k**). The individual similarity scores were written into a detection map (**Supplementary Fig. 14e**). By applying a threshold of 0.5 to this detection map, only a few false positive were still detected. In a subsequent manual post-processing step, we removed the remaining false positives and joined detected centers in consecutive frames that belonged to the same rosette. Further details are given in the **Supplementary Note**.

**Statistical analysis.** Statistical analysis was performed using SigmaStat (Systat Software). Circular statistics and rose plots were generated in Oriana 2.0 (Kovach Computing Service). The frequency of observations in rose plots is represented by the area of each wedge. The concentric circles correspond to the observed frequencies. The Mardia-Watson-Wheeler test determines the probability that two samples are from the same population of angular measurements. It was used to determine a difference between circular distributions, with signficance defined as $P < 0.05$. All experiments were repeated at least three times.

26. Rabut, G. & Ellenberg, J. Automatic real-time three-dimensional cell tracking by fluorescence microscopy. *J. Microsc.* **216**, 131–137 (2004).
27. Kolega, J. Phototoxicity and photoinactivation of blebbistatin in UV and visible light. *Biochem. Biophys. Res. Commun.* **320**, 1020–1025 (2004).
28. Avants, B.B., Epstein, C.L., Grossman, M. & Gee, J.C. Symmetric diffeomorphic image registration with cross-correlation: evaluating automated labeling of elderly and neurodegenerative brain. *Med. Image Anal.* **12**, 26–41 (2008).
29. Brox, T., Bruhn, A., Papenberg, N. & Weickert, J. High accuracy optical flow estimation based on a theory for warping. *European Conference on Computer Vision (ECCV)* Vol. 3024 of. *LNCS* 25–36 (2004).
30. Otsu, N. A threshold selection method from gray-level histograms. *IEEE Trans. Sys. Man Cyber.* **9**, 62–66 (1979).

# Supplementary Figures and Supplementary Note to:

# Vertebrate kidney tubules elongate using a planar cell polarity-dependent, rosette-based mechanism of convergent extension

Soeren S. Lienkamp[1], Kun Liu[2,5], Courtney M. Karner[3,4], Thomas J. Carroll[3,4], Olaf Ronneberger[2,5], John B. Wallingford[6,7] & Gerd Walz[1,5]

[1]Renal Division, Department of Medicine, University of Freiburg Medical Center, Hugstetter Straße 55, 79106 Freiburg, Germany

[2]Image Analysis Lab, Department of Computer Science, University of Freiburg, Georges-Koehler-Allee 52, 79110 Freiburg, Germany

[3]Department of Internal Medicine, Division of Nephrology, University of Texas Southwestern Medical Center, Dallas, Texas, USA.

[4]Department of Molecular Biology, University of Texas Southwestern Medical Center, Dallas, Texas, USA.

[5]Centre for Biological Signalling Studies (BIOSS), Albertstraße 19, 79104 Freiburg, Germany

[6]Howard Hughes Medical Institute; Section of Molecular Cell and Developmental Biology; University of Texas, Austin, Texas 78712, USA

[7]Institute for Cellular and Molecular Biology, University of Texas, Austin, Texas 78712, USA

Correspondence should be addressed to J.B.W (wallingford@mail.utexas.edu), or G.W. (gerd.walz@uniklinik-freiburg.de).
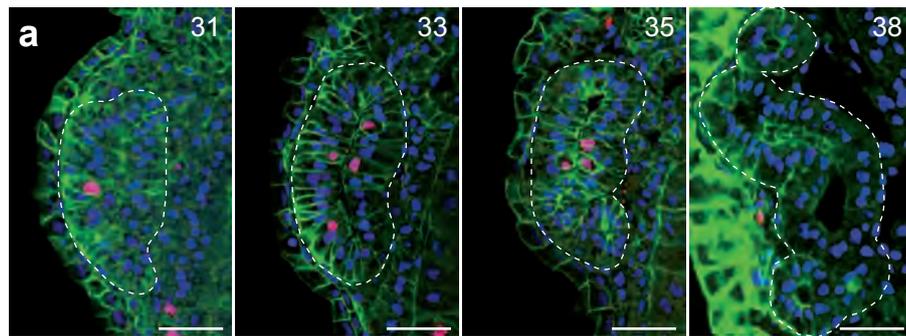
**a** memGFP p-Histone-H3 DAPI
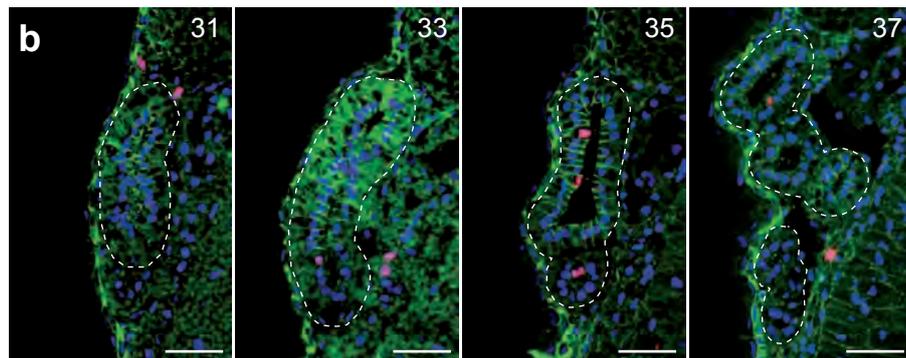
**b** beta-Cat p-Histone-H3 DAPI

**c** percentage of cells

**d**
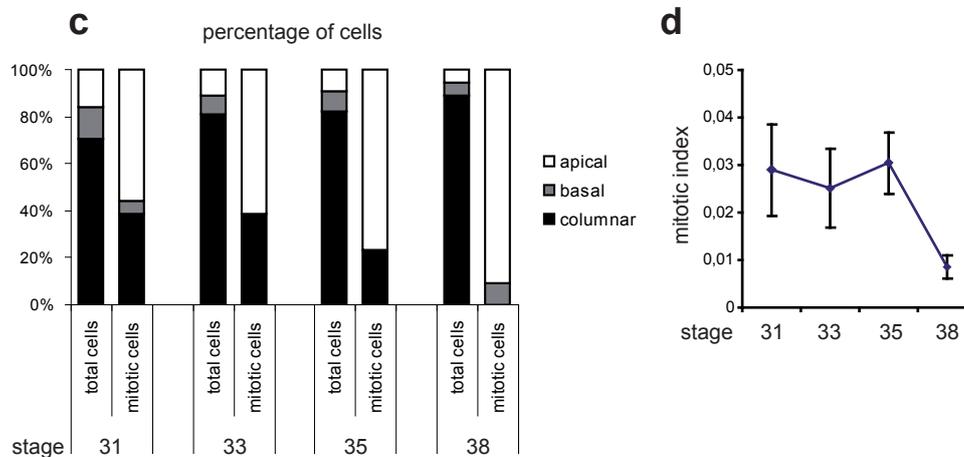
**Suppl. Figure 1 Lumen formation and apical mitosis in the Xenopus pronephros**
Lumen formation begins around stage 35. Xenopus embryos, expressing membrane-associated GFP (memGFP), were fixed at indicated stages with anti-phopsho-histone-H3 (p-Histone-H3) and DAPI in combination with either **(a)** anti-GFP or **(b)** anti-β-catenin before sectioning (5μm plastic sections). The pronephros is outlined by a broken line. Scale bar, 50 μm. **(c)** Cells were classified by position within the epithelium. Apical and basal cells do not reach the opposing epithelial side, while columnar shaped cells extent from the basal side to the apical surface. Increasing numbers of mitotic cells are found at the apical side as development progresses, indicative of a pseudo-stratified epithelium. **(d)** The mitotic index declines towards stage 38 (error bars, SEM). A total of 7-8 embryos were analyzed for each stage.
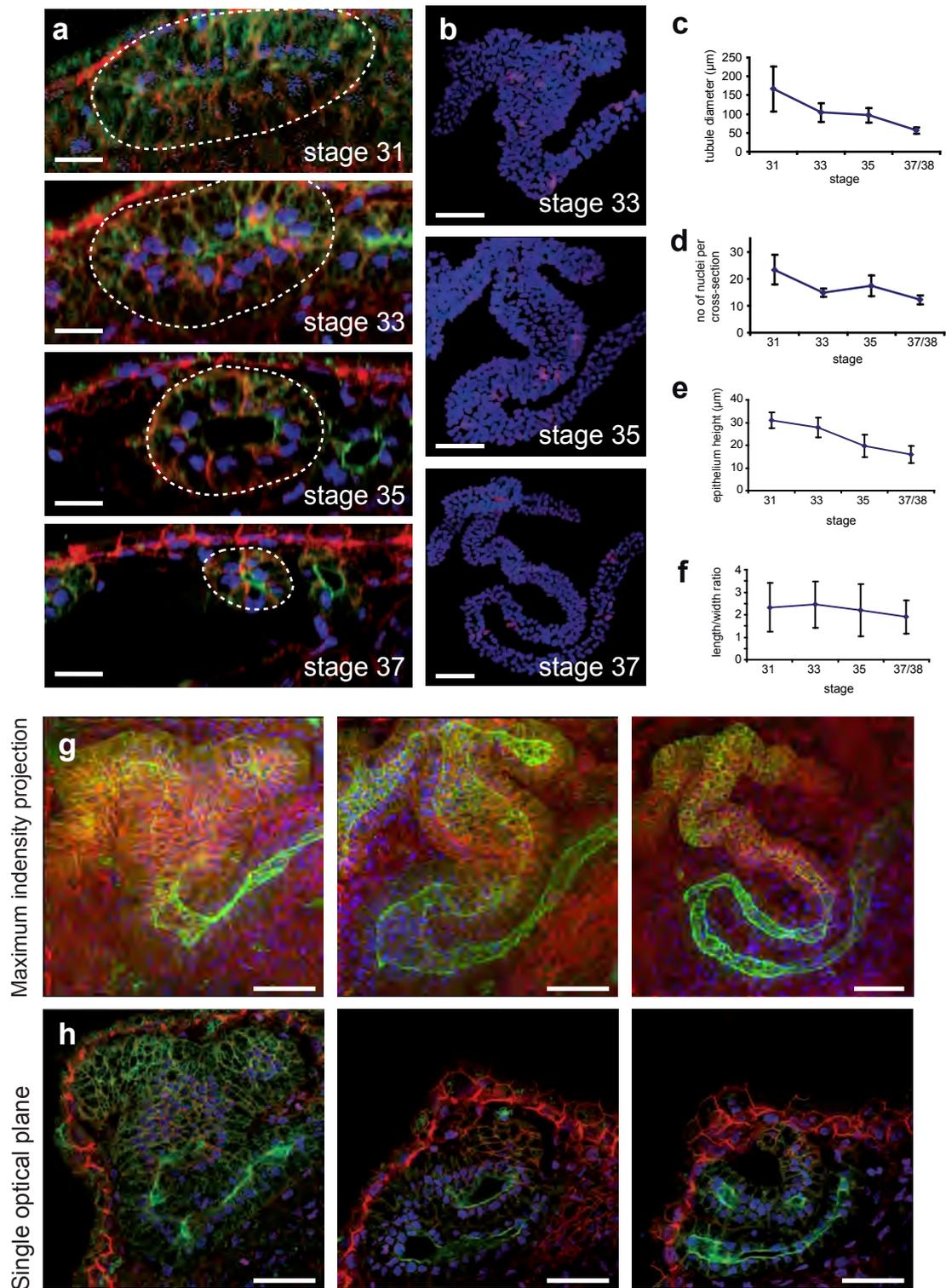
**Suppl. Figure 2 The tubule diameter decreases as fewer cells form the tubule diameter**
Confocal stacks of Xenopus embryos were stained with anti-β-catenin (red), tomato-lectin (green) and DAPI (blue), and anti-phospho-histone H3 (purple). **(a)** Optical cross-sections were positioned perpendicular to the tubule of the proximal segment at indicated stages. The tubules are outlined by white broken lines. Scale bar, 20 μm. **(b)** Mitotic cells (red) are found in all segments. Scale bar 50 μm. **(c)** Decrease of tubular diameter over time. **(d)** Decreasing number of cells per diameter. **(e)** The epithelium flattens during development. **(f)** The length-width ratio of tubule epithelial cells remains constant. Error bars for all graphs: SEM **(g)** Maximum intensity projections of images in Fig. 2b,c,d without cell rendering. **(h)** Single optical planes to visualize cell boundaries that were used to 3D render cells in Fig. 2b,c,d. Scale bar, 50 μm.
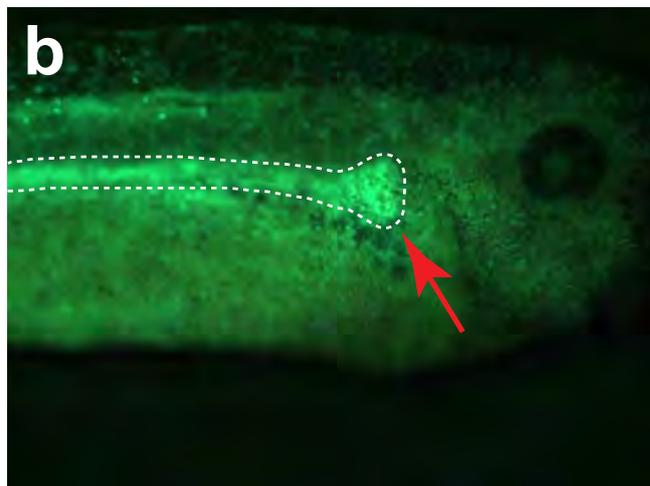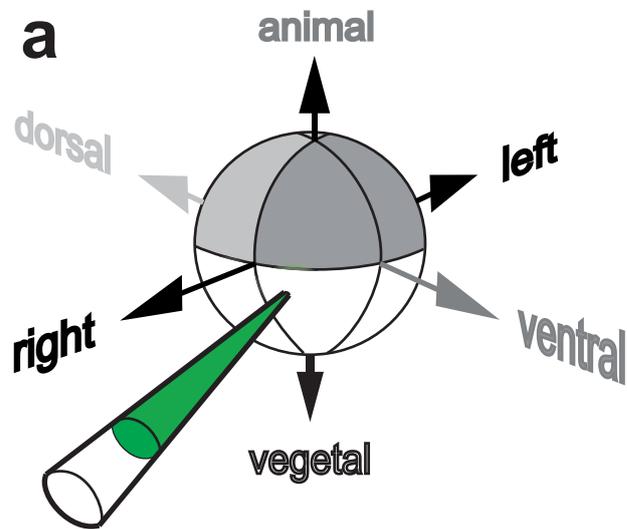
**Suppl. Figure 3 Targeted injection for tissue limited expression of fluorescent proteins**
**(a)** Schematic depiction of a Xenopus embryo at the 8-cell stage. Injections were performed into the lateral-vegetal blastomeres. **(b)** Expression of GFP is predominantly limited to the pronephros of the stage 36 tadpole (outlined by a broken line, red arrow).
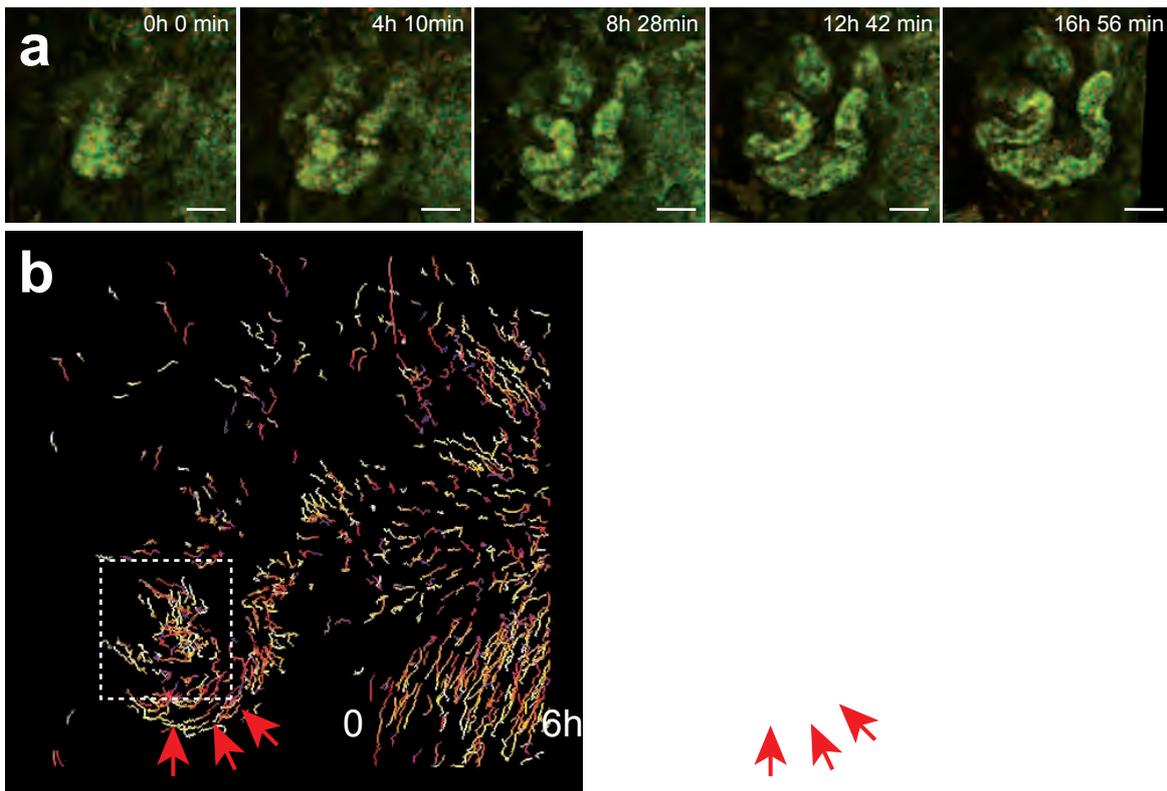
**Suppl. Figure 4 Time-lapse imaging of pronephros morphogenesis**
**(a)** Maximum intensity projections of confocal time-lapse recordings after expression of membrane-GFP and histone H3-RFP in the Xenopus pronephros is shown for the duration of 16 hours and 56 minutes. Scale bar, 100 μm. **(b)** Automated detection and tracking of nuclei was performed to visualize morphogenetic movements. Time-coded movement tracks of single nuclei reveal the cell movements during renal tubule development. **(c)** Displacement vectors indicate the start and ending postion of tracks in (b) independent of velocity. The complex cell rearrangements during tubule narrowing of the proximal tubule (white broken box) are highlighted. Red arrows highlight anterior movement of cells in the intermediate segment.

**a** Tissue elongation by remodelling of 4-cell junctions

Type 1 → Type 2 → Type 3
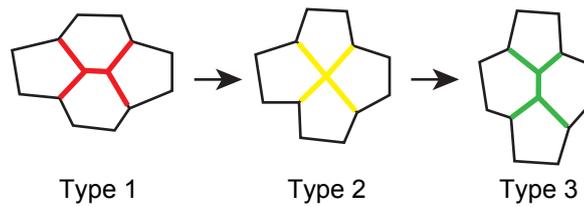
**b** Proportion of 4-cell junctions over time
WT (n=3 tubules)

Type 1
Type 2
Type 3
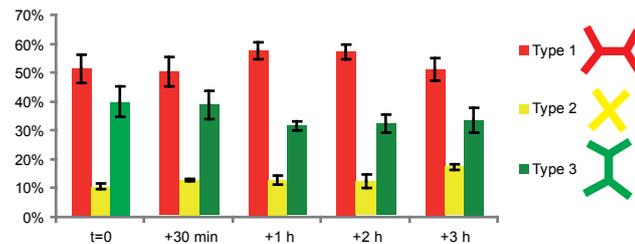
**c** Wild type Type 2 Junction

Formation    Resolution
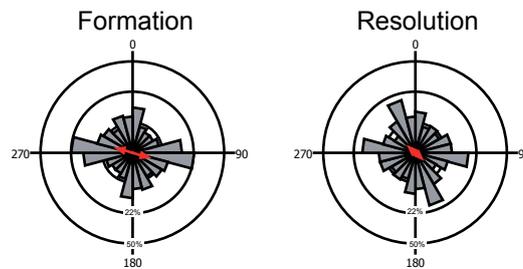
**d** Proportion of 4-cell junctions over time
Xdd1-GR (n=3 tubules)
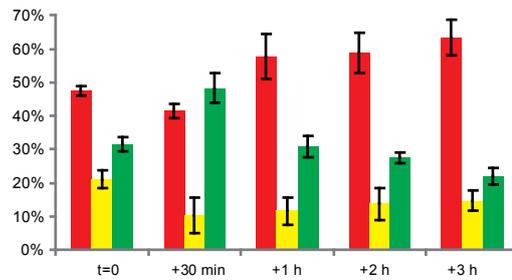
**e** Xdd1-GR Type 2 Junction

Formation    Resolution
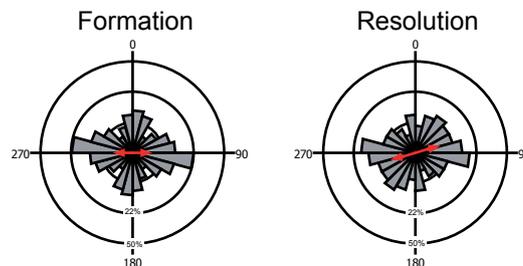
**Suppl. Figure 5 The formation and resolution of 4-cell junctions is not polarized**
**(a)** Diagram of a potential tissue elongation mechanism based on 4-cell remodeling. **(b)** Distribution of type 1, 2 and 3 junctions over time in wild type and **(c)** The angular distribution of formation and resolution of type 2 junctions is not significantly biased (p=0,4, Mardia-Watson-Wheeler test, n= 90 type-2 junctions in 3 tubules). **(d)** Xdd1-GR expressing tubules (n=3 tubules). Type 1 junctions are horizontally aligned to the longitudinal axis of the tubule. Type 2 junctions of 4 meeting cells. Type 3 junctions are vertically aligned. No progression towards type 3 junctions is observed. **(e)** The resolution angle of Xdd1-GR expressing tubules. (p=0.6, n= 46 type-2 junctions in 3 tubules). Red arrows indicate the mean angle.
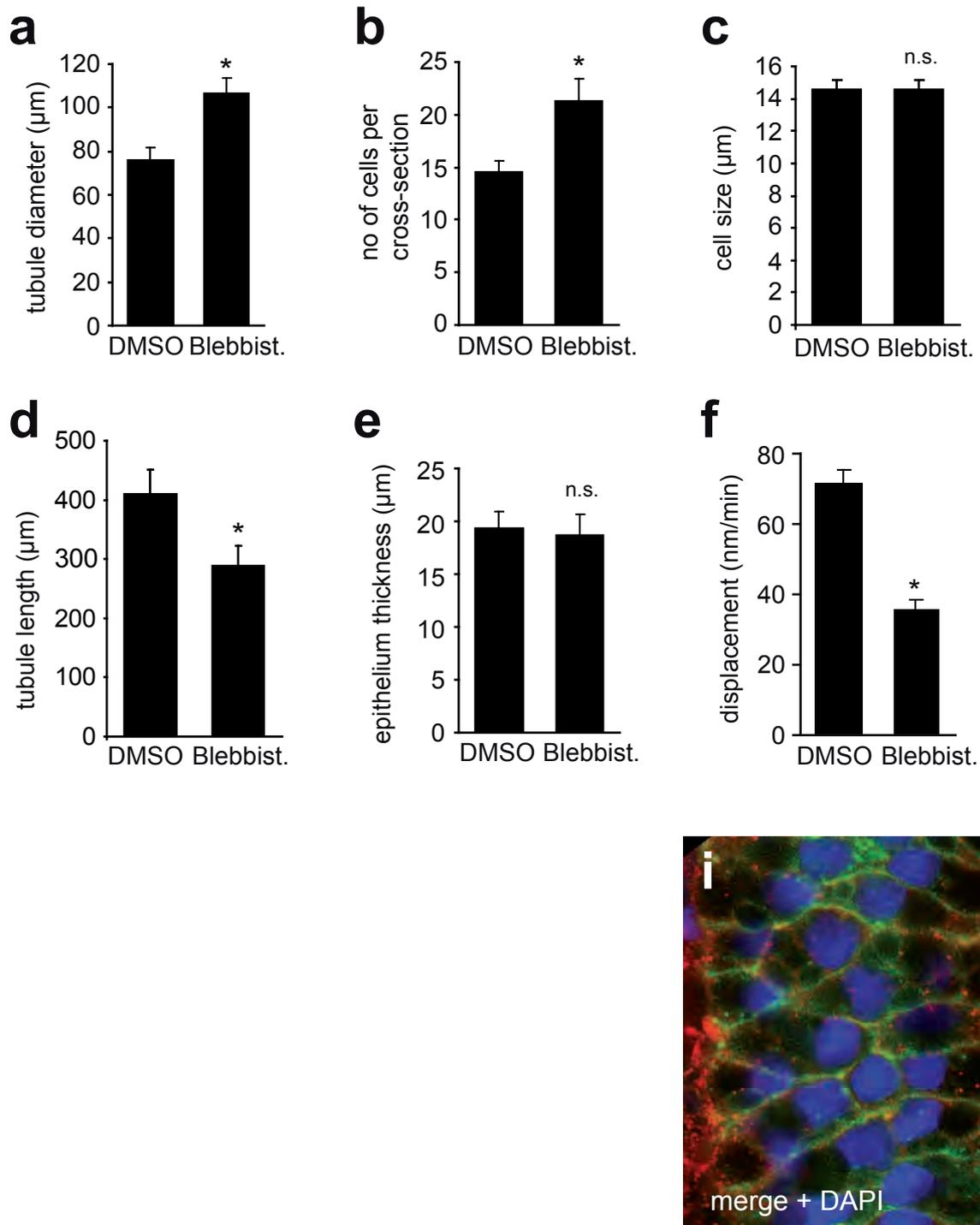
**Suppl. Figure 6 Blebbistatin treatment has profound effects on tubule morphogenesis and rosette formation:** **(a)** The tubule diameter is enlarged after treatment with blebbistatin (Blebbist.). **(b)** The number of cells contributing to the tubule circumference is increased. **(c)** Cell size, measured as the maximum diameter of the basal surface in mediolateral direction is not significantly different. **(d)** Tubule length was determined from the confluence of the neph-rosomes to the anterior part of the intermediate segment (see yellow line in Fig.4a,b) and is significantly reduced. **(e)** The epithelium thickness is unchanged in blebbistatin treated embryos. (n.s. not significant, *p < 0.05, t-test, n=13 DMSO treated embryos, n=16 blebbistatin treated embryos.) **(f)** the displacement speed is significantly reduced in tracked cells (*p<0.01; DMSO: n=161; blebbistatin: n=176 cells in 3 parallel imaged embroys; error bars: SEM in all graphs). **(g)** Xenopus embryos were stained for phosphor-Myosin light chain, and Tomato lectin **(h)** visualizing the cell membranes in renal tubules. Arrows indicate where intensity measurements were taken. The angles were taken in relationship to the tubular lumen. (proximal to the top and distal to the bottom). **(i)** Merged image of (g) and (h) inclu-ding the DAPI channel.

**a** Multi-cellular rosettes in wildtype
and Wnt9b mutant mouse kidneys



**b** Multi-cellular rosettes in wildtype
and Xdd1-GR *Xenopus* kidneys
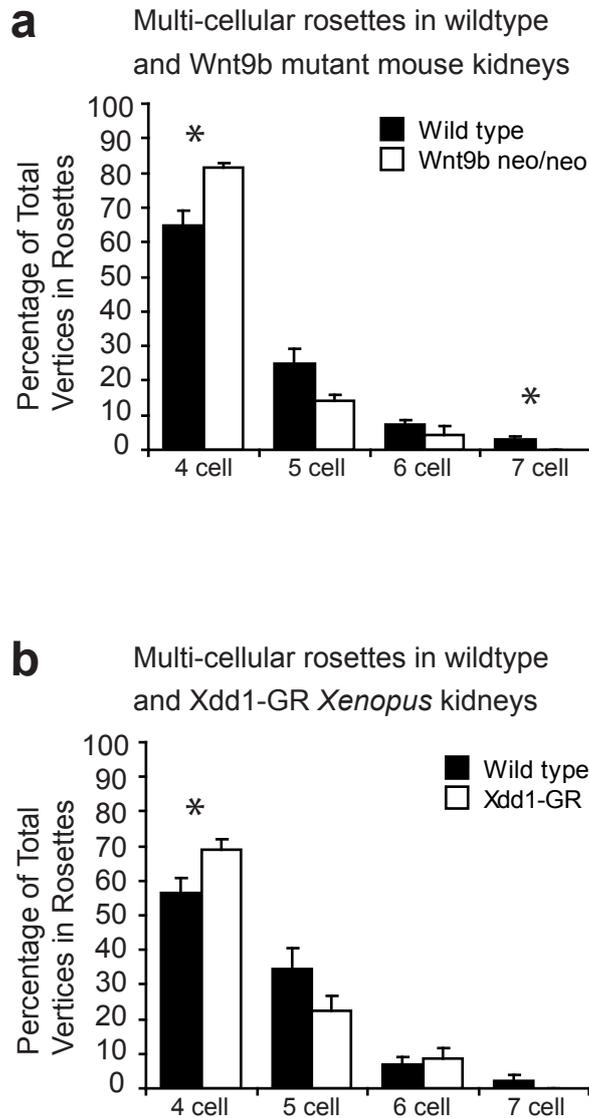


**Suppl. Figure 7 Rosette formation in Wnt9b deficient mice and Xdd1 expressing Xenopus tubules**
**(a)** The quantitative analysis of the number of cells participating in rosette formation reveals a shift towards lower order rosettes in Wnt9bneo/neo kidneys in comparison to wild type kidneys. (Wnt9bneo/neo: n=212 rosettes; wild type: n=263 rosettes in 3 embryos, *p<0.05, t-test, error bars: SEM) **(b)** The quantitative analysis of rosettes in fixed Xenopus renal tubules at stage 37 reveals a similar shift towards lower order rosettes in Xdd1-GR expressing kidneys (Xdd1-GR: n=97 rosettes, wild type: n= 96 rosettes in 7 embryos; *p < 0.05, t-test, error bars: SEM).
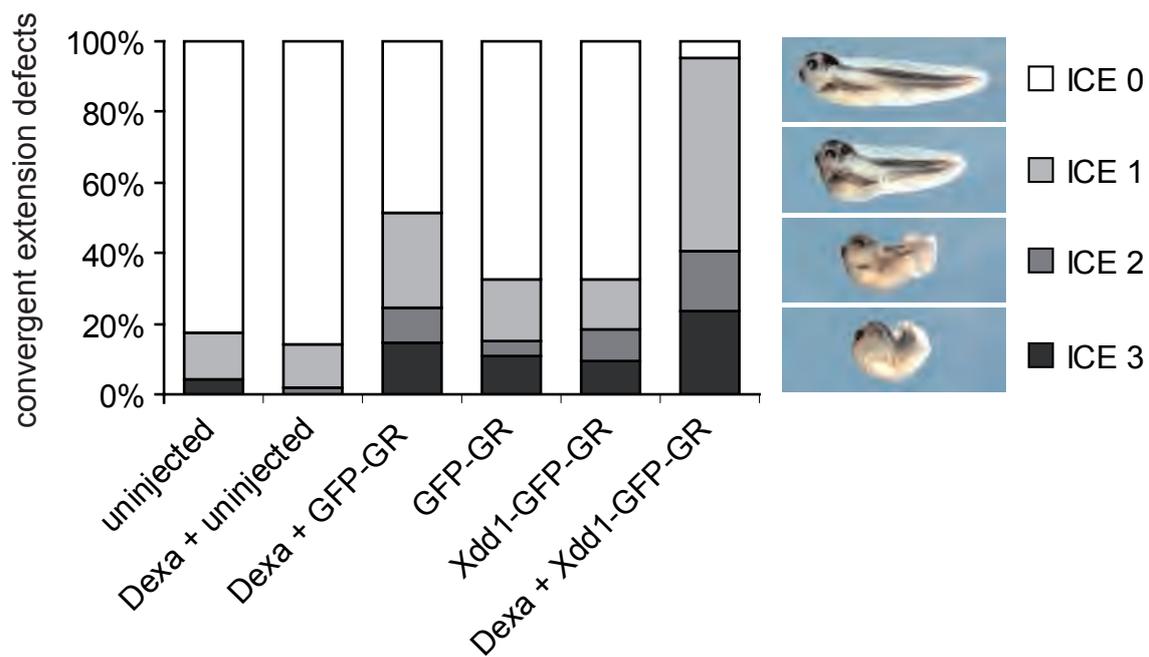
**Suppl. Figure 8 Effect of Xdd1-GR expression on convergent extension.**
Both dorsal blastomeres of Xenopus embryos were injected at the 4-cell stage with RNA coding for a fusion protein of Xdd1 and the human growth-hormone receptor (Xdd1-GR). The shortened axis scored as depicted at stage 36-40 (ICE: impaired convergent extension). In the presence of dexamethasone (Dexa, activating hormone of Xdd1-GR) the defects were strongest, while dexamethasone treatment alone had no effect on development of Xenopus embryos (n= 41 to 49 embryos in each group) .
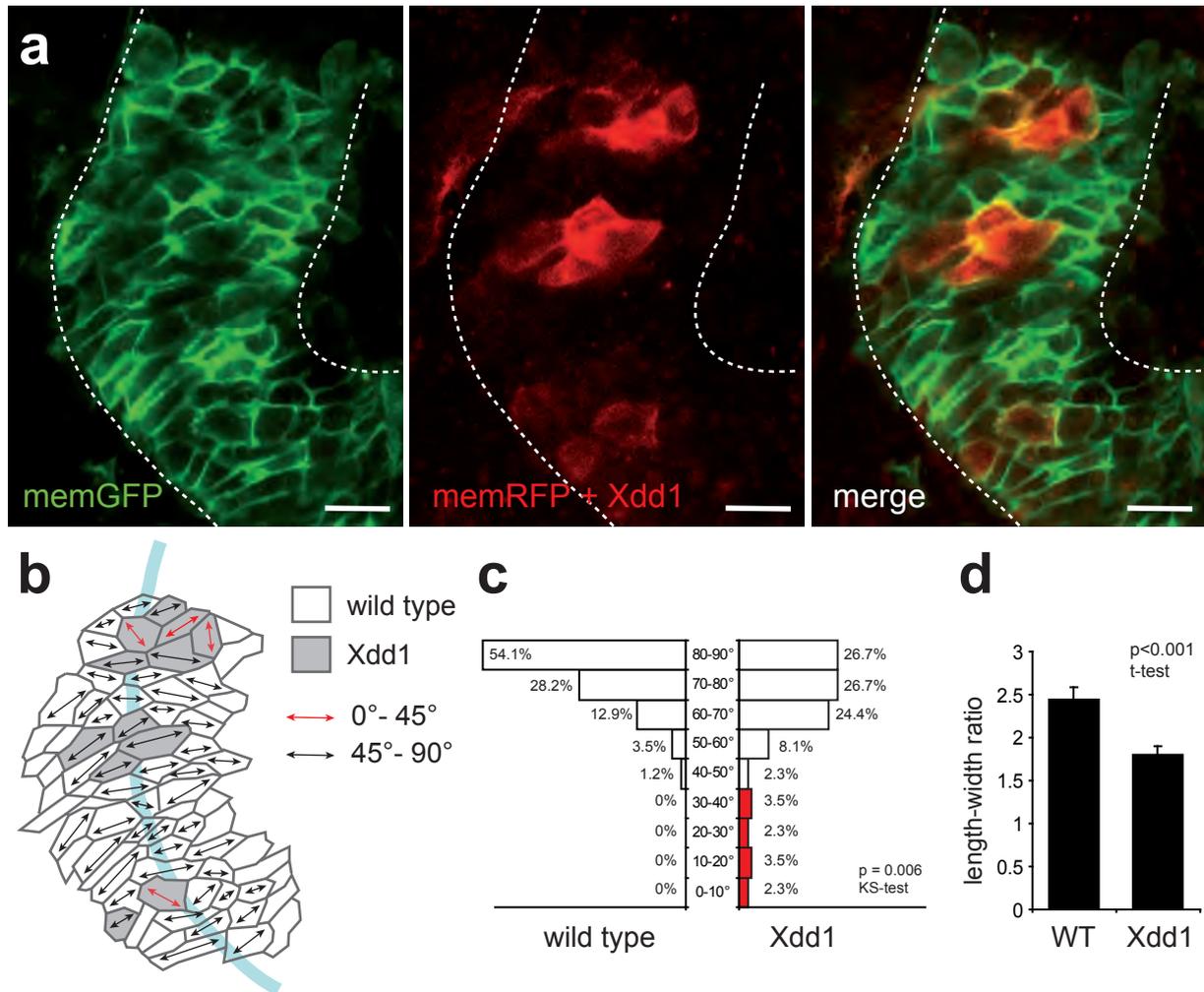
**Suppl. Figure 9 Cell elongation and orientation is influenced by Xdd1**
**(a)** Xdd1, a dominant-negative Dishevelled mutation that specifically interferes with planar cell polarity signaling, is expressed in a subset of tubular epithelial cells labeled by membrane-associated RFP (memRFP, red) in Xenopus embryos. All other tubular epithelial cells (wild type) are marked by membrane-associated GFP (memGFP, green). Scale bar, 20 µm. **(b)** The angle of the longest cell diameter was measured. Red arrows indicate and angle in relationship to the longitudinal axis of the tubule (blue line) between 0 and 45°; a gray arrow labels cells with an angle between 45 and 90°. **(c)** The distribution of angles reveals that more Xdd1-expressing cells are oriented in angles <45° in relationship to the tubule axis (wild type cells, n=85 measurements at hourly intervals of 19 cells; Xdd1-positive cells, n=86 measurements of 20 cells; p=0.006). **(d)** The length-width ratio is decreased by Xdd1 (p<0.001, t-test, error bars: SEM).
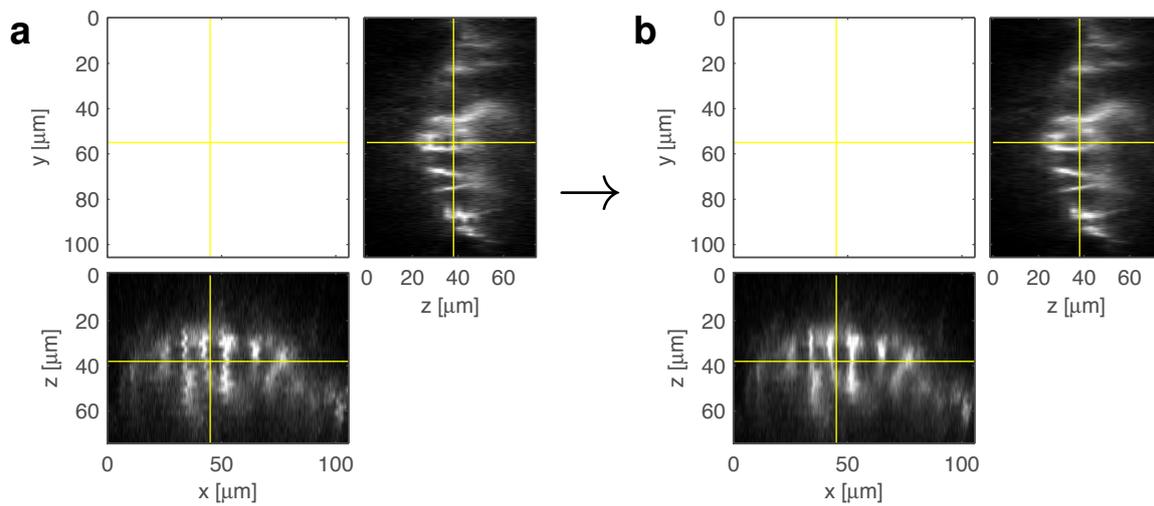
**Supplementary Figure 10** │ Heart beat compensation: (**a**) Raw data shows significant artefacts due to fast pulsation of the sample during confocal scanning (most notable here in the xz-slice). (**b**) After compensation by elastic registration of subsequent slices these artefacts are removed
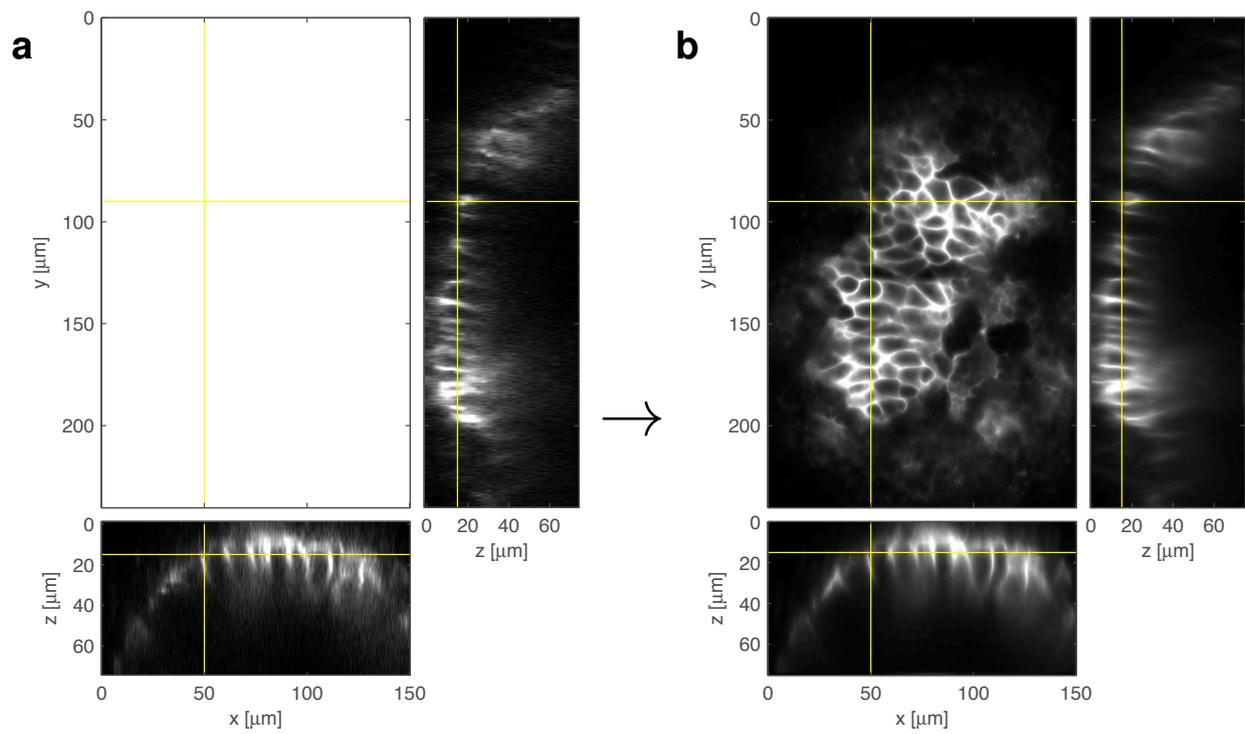
**Supplementary Figure 11** │ Anisotropic diffusion for cell border enhancement and denoising: (**a**) raw data, (**b**) filtered data
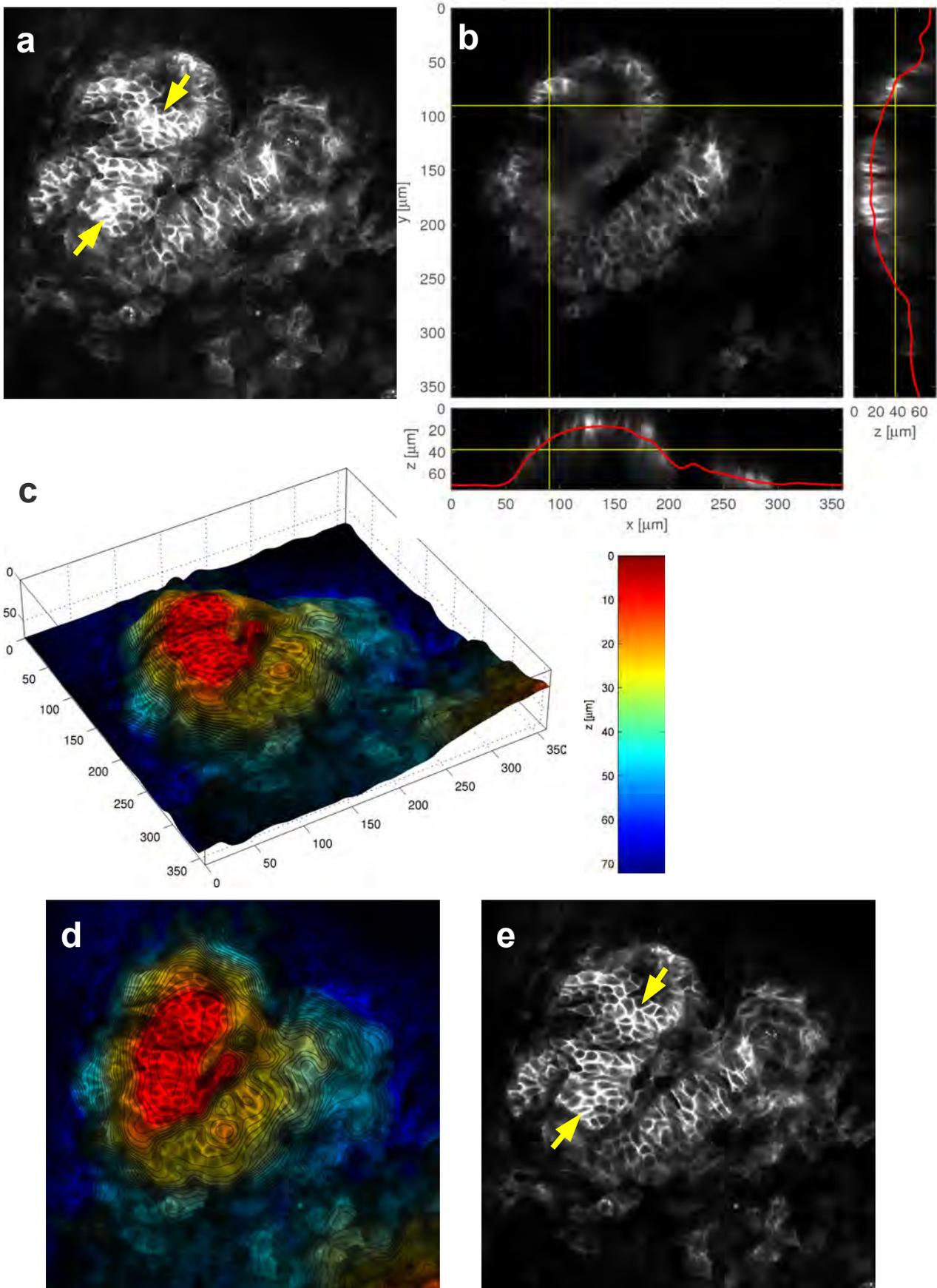
**Supplementary Figure 12** | Cell layer extraction: (**a**) Maximum intensity projection of raw image stack. (**b**) Orthogonal slices of filtered image stack. The red lines indicate the detected cell layer. (**c**) 3D rendering of the extracted cell layer. The color and the contour lines depict the z-position in the data set. (**d**) Extracted slice with color code and contour lines. (**e**) Extracted slice for further processing. Cell borders are clearly visible.
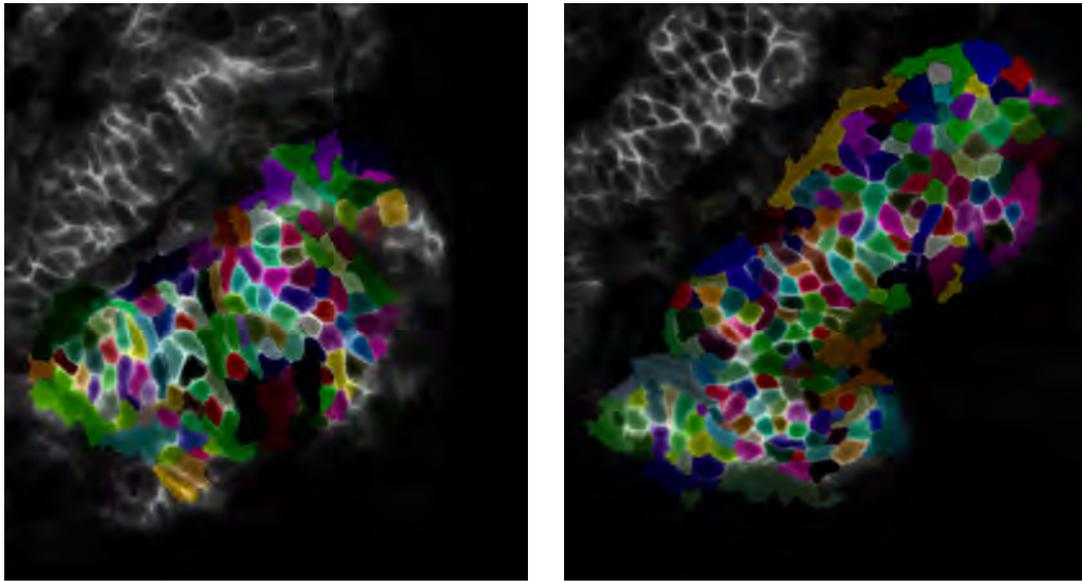
**Supplementary Figure 13** | Automatic cell segmentation: two frames of random-colored segmentation masks overlaid on the enhanced images. This result comes from a marker-controlled watershed and the voting from neighboring frames, which are aligned based on the optical flow.
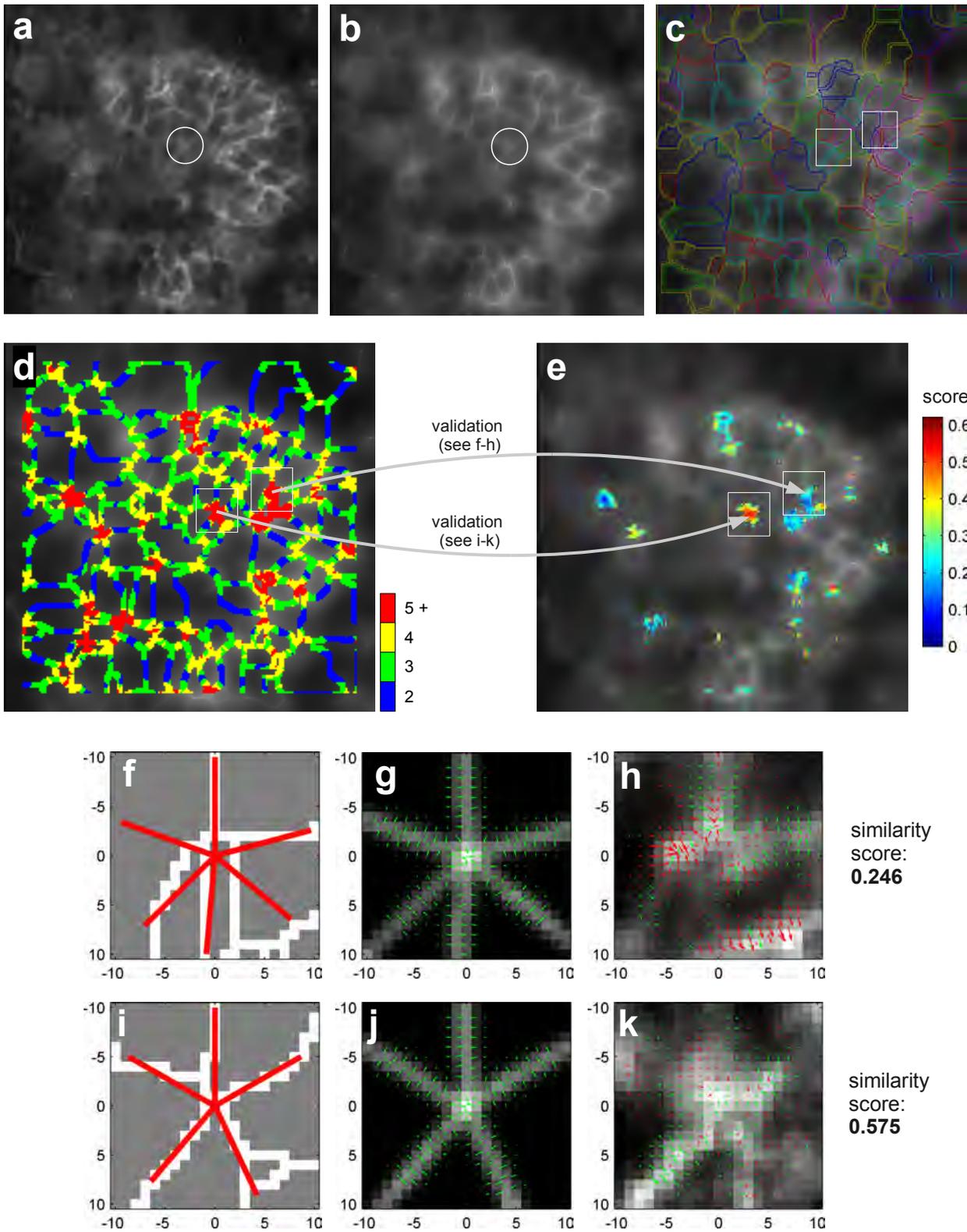
**Supplementary Figure 14** │ Rosette Detection: (**a**) Cell layer extracted from raw image. (**b**) Cell layer extracted from filtered image. (**c**) Over-segmentation by watershed. Two rosette center candidates are depicted by white squares (**d**) Rosette center candidates. The color indicates the number of segments in the surrounding. Two of these candidates are depicted by a white square (**e**) Final detection score after validation. (**f-k**) Validation of candidates with the star-shaped rosette model: (**f**) Best fitting rosette model, given the watershed lines. (**g**) Synthetic rosette image. Gradient vectors are overlaid in green (**h**) Raw image at validation position. Gradient vectors of raw image are shown in red and green, where green indicates a match of the gradient direction with the synthetic image. (**i-k**) Analog images as in f-h but for a different position.

# Supplementary Note

## Notation

Images are denoted as continuous functions that map a given coordinate to the intensity at this point. Usually, 2D images are defined on a rectangular-shaped domain $\Omega \subset \mathbb{R}^2$ and 3D (volumetric) images are defined on a cuboid shaped domain $\Omega \subset \mathbb{R}^3$. A typical example for an Image is $I : \Omega \to \mathbb{R}; \mathbf{x} \mapsto I(\mathbf{x})$ with $\mathbf{x} \in \Omega$ and $I(\mathbf{x}) \in \mathbb{R}$.

## Heart Beat Compensation

The confocal microscope scans the sample line-by-line and plane-by-plane. Therefore the time difference of two neighboring pixels in x-direction is in the range of microseconds, in y-direction in the range of milliseconds and in z-direction in the range of seconds (assuming an image size of approx. 1000x1000 in xy-direction). As the heart beat frequency is approx. 2-3 beats per second, the periodic deformations produce severe discontinuities of the structures in z-direction (Supplementary Fig. 10a). We compensate the discontinuities by an elastic deformation of each slice: For this, the image stack is described by a set of $N$ 2D slices $S_i : \mathbb{R}^2 \to \mathbb{R}; \mathbf{x} \mapsto S_i(\mathbf{x}); i \in \{1, \ldots, N\}$. For each pair of subsequent slices the pixel correspondences are found by a dense diffeomorphic registration [1], such that

$$S_i(\mathbf{x}) = S_{i+1}(\mathbf{x} + \mathbf{F}_i(\mathbf{x})), \tag{1}$$

where $\mathbf{F}_i : \mathbb{R}^2 \to \mathbb{R}^2; \mathbf{x} \mapsto \mathbf{F}_i(\mathbf{x})$ is the forward deformation field. Due to the diffeomorphism the inverse deformation $B_{i+1} := F_i^{-1}$ always exists. We denote the backward deformation field as $\mathbf{B}_i : \mathbb{R}^2 \to \mathbb{R}^2; \mathbf{x} \mapsto \mathbf{B}_i(\mathbf{x})$, such that

$$S_i(\mathbf{x}) = S_{i-1}(\mathbf{x} + \mathbf{B}_i(\mathbf{x})). \tag{2}$$

After all $F_i$ and $B_i$ are computed for each pair of slices, the relation of three subsequent slices can be written as

$$S_{i-1}(\mathbf{x} + \mathbf{B}_i(\mathbf{x})) = S_i(\mathbf{x}) = S_{i+1}(\mathbf{x} + \mathbf{F}_i(\mathbf{x})). \tag{3}$$

The optimal deformation $\mathbf{U}_i : \mathbb{R}^2 \to \mathbb{R}^2$ for each slice (considering the two neighboring slices) is found by applying a small filter with the kernel $K = (\frac{1}{4}, \frac{1}{2}, \frac{1}{4})$ to the displacements. The displacement of the slice $S_i$ to itself is zero, so the optimal resulting deformation field is:

$$\mathbf{U}_i(\mathbf{x}) = \frac{1}{4}\mathbf{F}_i(\mathbf{x}) + \frac{1}{4}\mathbf{B}_i(\mathbf{x}). \tag{4}$$

To corrected slice is then

$$S_{\text{corrected},i}\left(\mathbf{x} + \mathbf{U}_i(\mathbf{x})\right) = S_i(\mathbf{x}). \tag{5}$$

The result is shown in Supplementary Fig. 10b.

## Cell border enhancement and Denoising

The anisotropic diffusion for cell border enhancement and denoising can be formulated in this partial derivative equation [5]:

$$\frac{\partial I(\mathbf{x})}{\partial t} = \text{div}(\mathbf{D}(\mathbf{x})\nabla I(x)), \tag{6}$$

where $\nabla$ indicates the gradient of image, and $\text{div}$ is the divergence. The diffusion behavior is controlled by the diffusion tensor $\mathbf{D} : \Omega \to \mathbb{R}^{3\times 3}; \mathbf{x} \mapsto \mathbf{D}(\mathbf{x})$. The diffusion result after a certain time can be computed by an explicit time integral. It is well-known that the Hessian matrix (second-order derivatives) is very effective for featuring plan-like structures [4], so it is used here to construct the diffusion tensor, which drives the diffusion

process in the anisotropic way. Let the eigenvalues of the local Hessian matrix be $\ell_1 > \ell_2 > \ell_3$, and their corresponding eigenvectors be $\mathbf{v}_1, \mathbf{v}_2, \mathbf{v}_3$, then the diffusion tensor is constructed as

$$\mathbf{D} = e^{-(\min(\ell_1,0)/\kappa)^2}\mathbf{v}_1\mathbf{v}_1^T + e^{-(\min(\ell_2,0)/\kappa)^2}\mathbf{v}_2\mathbf{v}_2^T + e^{-(\min(\ell_3,0)/\kappa)^2}\mathbf{v}_3\mathbf{v}_3^T. \tag{7}$$

The parameter $\kappa$ is optimized manually to obtain clear cell borders within the tubule structures. The effect of this diffusion tensor can be explained as follows: it suppresses the diffusion along the directions in which $\ell$ is large compared to $\kappa$ (which means there is a bright border), and allows strong diffusion along the directions in which there are no clear border. The effect of the enhancement is illustrated in Supplementary Fig. 11.

## Cell layer extraction

The local z-position of the curved single cell-layer (Supplementary Fig. 12b-e) is estimated in the filtered image by searching the position with the sharpest edges (highest gradient magnitude) while keeping the layer smooth. The filtered volumetric image is denoted as $I : \mathbb{R}^3 \to \mathbb{R}$. The edge score $E : \mathbb{R}^3 \to \mathbb{R}$ is computed from the $x$ and $y$ component of the gradient as

$$E(x,y,z) = \sqrt{\left(\frac{\partial}{\partial x}I\right)^2(x,y,z) + \left(\frac{\partial}{\partial y}I\right)^2(x,y,z)}. \tag{8}$$

Then the edge information (originating mainly from the cell borders) is spread into the local surrounding by filtering with a "flat" Gaussian kernel

$$G_1(x,y,z) = e^{-\left(\frac{x^2+y^2}{\sigma_{xy}^2} + \frac{z^2}{\sigma_z^2}\right)}, \tag{9}$$

with $\sigma_{xy} = 15\mu$m and $\sigma_z = 2\mu$m. Finally the z-position of the maximal score is determined for each $(x,y)$ position,

$$Z_{\text{opt}}(x,y) = \arg\max_z (G_1 * E)(x,y,z), \tag{10}$$

and filtered with a Gaussian kernel $G_2$ with $\sigma_{xy} = 15\mu$m to obtain a smooth shape without jumps in $z$-direction:

$$Z_{\text{final}}(x,y) = (G_2 * Z_{\text{opt}})(x,y) \tag{11}$$

The extracted cell layer $S : \mathbb{R}^2 \to \mathbb{R}$ is then

$$S(x,y) = I\left(x,y,Z_{\text{final}}(x,y)\right). \tag{12}$$

## Drift Compensation (Stabilization)

The displacement of two successive data sets $I_t : \mathbb{R}^3 \to \mathbb{R}$ and $I_{t+1} : \mathbb{R}^3 \to \mathbb{R}$ is estimated by a normalized cross correlation of their maximum intensity projections $M_t : \mathbb{R}^2 \to \mathbb{R}$ and $M_{t+1} : \mathbb{R}^2 \to \mathbb{R}$.

$$N_{\text{CC},t}(\mathbf{d}) = \frac{\int_\Omega \left( M_t(\mathbf{x}) - \overline{M_t} \right) \cdot \left( M_{t+1}(\mathbf{x} + \mathbf{d}) - \overline{M_{t+1}}(\mathbf{d}) \right) d\mathbf{x}}{\sqrt{\left( \int_\Omega \left( M_t(\mathbf{x}) - \overline{M_t} \right)^2 d\mathbf{x} \right) \cdot \left( \int_\Omega \left( M_{t+1}(\mathbf{x} + \mathbf{d}) - \overline{M_{t+1}}(\mathbf{d}) \right)^2 d\mathbf{x} \right)}} \tag{13}$$

with

$$\overline{M_t} := \frac{1}{|\Omega|} \int_\Omega M_t(\mathbf{x}) d\mathbf{x} \tag{14}$$

$$\overline{M_{t+1}}(\mathbf{d}) := \frac{1}{|\Omega|} \int_\Omega M_{t+1}(\mathbf{x} + \mathbf{d}) d\mathbf{x} . \tag{15}$$

The best displacement is determined by the maximum of $N_{\text{CC}}$ as

$$\mathbf{d}_{\text{best},t} = \arg \max_{\mathbf{d}} N_{\text{CC},t}(\mathbf{d}) . \tag{16}$$

The stabilization of the whole time series is then performed by transforming each frame $S_t : \mathbb{R}^2 \to \mathbb{R}$ with the cumulated displacements,

$$S_{\text{stab},t}(\mathbf{x}) = S_t \left( \mathbf{x} + \sum_{i=1}^{t-1} \mathbf{d}_{\text{best},i} \right) . \tag{17}$$

## Semi-automated Cell Tracking

The cell tracking is performed on the stabilized cell layer slices $S_{\text{stab},t} : \Omega \to \mathbb{R}$, with $\Omega \subset \mathbb{R}^2$ and $t \in \{1, \ldots, T\}$, that were extracted from the filtered images. The cell centers in the last frame $S_{\text{stab},T}$ are found by searching for local gray value minima

$$\mathcal{M} = \left\{ \mathbf{x} \in \Omega : S_{\text{stab},T}(\mathbf{x}) < S_{\text{stab},T}(\mathbf{n}) \wedge 0 < \|\mathbf{n} - \mathbf{x}\| \leq \sqrt{2}g \ \ \forall \mathbf{n} \in \Omega \right\} , \tag{18}$$

where $g \in \mathbb{R}$ denotes the pixel grid spacing in micrometer. To avoid double detections of the same cell, minima that are closer to a stronger minimum than the minimal cell diameter (here $4\mu$m) are removed. The potiential double detections of each detection $x$ are denoted as

$$\mathcal{D}(\mathbf{x}) = \left\{ \mathbf{y} \in \mathcal{M} : 0 < \|\mathbf{y} - \mathbf{x}\| \leq 4\mu\text{m} \right\} . \tag{19}$$

Then we can write the set of final detections as

$$\mathcal{M}' = \left\{ \mathbf{x} \in \mathcal{M} : \mathcal{D}(\mathbf{x}) = \emptyset \vee \left( S_{\text{stab},T}(\mathbf{x}) < S_{\text{stab},T}(\mathbf{n}) \ \ \forall \mathbf{n} \in \mathcal{D}(\mathbf{x}) \right) \right\} . \tag{20}$$

The tracking uses the backward optical flow. For the high quality datasets with low variation in the intensities the high accuracy optical flow [2] is used. For the datasets with greater variations in the image intensities a slightly less accurate but more robust method [1] using the locally normalized cross correlation as similarity measure was used for the flow computation.

The backward flow is denoted as $\mathbf{b}_t : \mathbb{R}^2 \to \mathbb{R}^2$. Each cell center is tracked back in time by searching for the trajectory that gives the best compromise between following the dense optical flow and passing through

the local gray value minima. The energy for a single trajectory, described by the position $\mathbf{x}_t$ for every time point is

$$E(\mathbf{x}_1, \ldots, \mathbf{x}_T) = \sum_{t=1}^{T-1} \left( \mathbf{x}_t - \left( \mathbf{x}_{t+1} + \mathbf{b}_{t+1}(\mathbf{x}_{t+1}) \right) \right)^2 + \lambda S_{\text{stab},t}(\mathbf{x}_t) \, . \tag{21}$$

The parameter $\lambda$ controls the relative weight the optical flow (term 1) and the image intensities (term 2). The global optimum of this energy is computed using dynamic programming and the fast squared distance transform of Felsenszwalb and Huttenlocher [3]. The global optimum over the whole time series often does not correspond to the correct cell trajectory, because only a few cells are visible in all frames. Therefore the energy was optimized piecewise, and superfluous parts of the trajectories were removed in a subsequent manual editing step. In a final validation step, all trajectories were manually inspected and corrected, if necessary.

## Rosette Detection

The rosette center candidate are found in an over-segmented image (see Online Methods and Supplementary Fig. 14c). For all rosette center candidates, the surrounding image patch $P : \mathbb{R}^2 \to \mathbb{R}$ (extracted from the raw image) is compared to a rosette model that consists of five (or more) radial rays with a length of $R = 7.5 \mu$m. This comparison is performed in two steps. In the first step the model parameters (angle of each ray) are determined as local maxima of the radial intensity sum of the watershed line image $W$ (see Supplementary Fig. 14f and i)

$$p(\varphi) = \int_0^R W(\varphi, r) \, dr \tag{22}$$

$$\mathcal{A} = \{ \varphi \mid p'(\varphi) = 0 \wedge p''(\varphi) < 0 \} \, . \tag{23}$$

To remove double detections of a single cell wall, all detections that are closer than $\varphi_{\min} = 30°$ to a neighboring stronger detection are removed:

$$\mathcal{A}_{\text{final}} = \{ \varphi \mid \varphi \in \mathcal{A}; \ \beta \in \mathcal{A}; \ |(\varphi - \beta) \bmod 2\pi| > \varphi_{\min} \ \vee \ p(\varphi) > p(\beta) \} \, . \tag{24}$$

Using the angles in the set $\mathcal{A}_{\text{final}}$ a synthetic image patch $M : \mathbb{R}^2 \to \mathbb{R}$ is rendered by drawing the rays and smoothing them with a Gaussian kernel $G_3$ with $\sigma = 0.75 \mu$m (Supplementary Fig. 14g and j)

$$L(\varphi, r) = \begin{cases} 1 & \text{if } \varphi \in \mathcal{A}_{\text{final}} \wedge r \leq R \\ 0 & \text{else} \end{cases} \tag{25}$$

$$M = G_3 * L \, . \tag{26}$$

Finally the synthetic and the real image patch are compared using a gradient based similarity metric that is robust to local intensity variations and additional small structures(Supplementary Fig. 14h and k). For this, we define the circular mask as $\Omega_c = \{ \mathbf{x} \in \mathbb{R}^2 \mid \|\mathbf{x}\| \leq R \}$, and specify a maximal angle between gradient vectors $\alpha_{\max}$ (here we use $\alpha_{\max} = 45°$). With the following definitions

$$P_{\text{gmag}} := \|\nabla P\| \qquad\qquad M_{\text{gmag}} := \|\nabla M\| \tag{27}$$

$$\mathbf{P}_{\text{gdir}} := \frac{\nabla P}{\|\nabla P\|} \qquad\qquad \mathbf{M}_{\text{gdir}} := \frac{\nabla M}{\|\nabla M\|} \tag{28}$$

$$\delta_{\text{dir}}(\mathbf{n}_1, \mathbf{n}_2) := \begin{cases} 1 & \text{if } \langle \mathbf{n}_1, \mathbf{n}_2 \rangle > \arccos(\alpha_{\max}) \\ 0 & \text{else} \end{cases} \tag{29}$$

we can write this similarity score $R$ as

$$R = \frac{\int_{\Omega_c} \delta_{\mathrm{dir}} \left( \mathbf{P}_{\mathrm{gdir}}(\mathbf{x}), \mathbf{M}_{\mathrm{gdir}}(\mathbf{x}) \right) \cdot P_{\mathrm{gmag}}(\mathbf{x}) \cdot M_{\mathrm{gmag}}(\mathbf{x}) \, d\mathbf{x}}{\sqrt{\left( \int_{\Omega_c} P_{\mathrm{gmag}}^2(\mathbf{x}) \, d\mathbf{x} \right) \cdot \left( \int_{\Omega_c} M_{\mathrm{gmag}}^2(\mathbf{x}) \, d\mathbf{x} \right)}} \, . \tag{30}$$

Similar to a normalized cross correlation this score ranges from 0 (no similarity) to 1 (perfect similarity). This comparison is computed for all rosette candidates and the resulting scores are written into a detection map (Supplementary Fig. 14e). By applying a threshold of 0.5 to this detection map, only few false positive detections are left. In a subsequent manual post-processing step, we removed remaining false-positive detections and joined detections in consecutive frames that belong to the same rosette.

# References

[1] B.B. Avants, C.L. Epstein, M. Grossman, and J.C. Gee. Symmetric diffeomorphic image registration with cross-correlation: Evaluating automated labeling of elderly and neurodegenerative brain. *Medical Image Analysis*, 12(1):26–41, February 2008.

[2] T. Brox, A. Bruhn, N. Papenberg, and J. Weickert. High accuracy optical flow estimation based on a theory for warping. In *European Conference on Computer Vision (ECCV)*, volume 3024 of *Lecture Notes in Computer Science*, pages 25–36. Springer, May 2004.

[3] P. Felzenszwalb and D. Huttenlocher. Distance transforms of sampled functions. Technical Report TR2004-1963, Cornell Computing and Information Science, 2004.

[4] Y. Sato, C.F. Westin, A. Bhalerao, S. Nakajima, N. Shiraga, S. Tamura, and R. Kikinis. Tissue classification based on 3d local intensity structures for volume rendering. *IEEE Transactions on Visualization and Computer Graphics*, 6(2):160–180, 2000.

[5] J. Weickert. *Anisotropic diffusion in image processing*. B.G. Teubner Stuttgart, 1998.